國 立 交 通 大 學

顯示科技研究所
碩 士 論 文

一維光子晶體奈米樑共振腔之研究

Investigation on One Dimensional Photonic Crystal Nanocavity
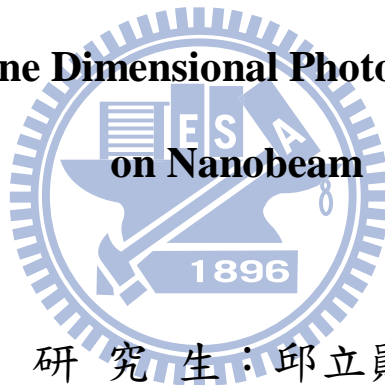
on Nanobeam

研 究 生：邱立勛

指導教授：李柏璁 教授

中 華 民 國 一 百 年 七 月

一維光子晶體奈米樑共振腔之研究

Investigation on One Dimensional Photonic Crystal Nanocavity on Nanobeam

研 究 生：邱立勛　　　　Student：Li-Hsun Chiu

指導教授：李柏璁　博士　　Advisor：Dr. Po-Tsung Lee

國 立 交 通 大 學

顯示科技研究所

碩 士 論 文

A Thesis

Submitted to Department of Photonic and Display Institute

College of Electrical Engineering and Computer Science

National Chiao Tung University

In partial Fulfillment of the Requirements

for the Degree of Master

in

Electro-Optical Engineering

July 2011

Hsinchu, Taiwan, Republic of China

中 華 民 國 一 百 年 七 月

一維光子晶體奈米樑共振腔之研究

研究生：邱立勛

指導教授：李柏璁 博士

國立交通大學光電工程學系顯示科技研究所碩士班

摘　　要

　　相較於二維光子晶體共振腔，一維光子晶體奈米樑共振腔不僅在元件有效面積上大幅的縮小了一個維度，更具有能與二維共振腔系統相匹的高品質因子(Q)及極小模態體積(V)等優越的模態特性，所以非常適合於在未來高密度積體光路中做為光源、感測器或特定功能元件的應用。

　　利用多重異質結構的模隙侷限效應，我們提出了兩種一維光子晶體奈米樑奈米共振腔結構設計(空氣孔洞中心及介電材料中心)，以有限元素法快速地找出對應的模態分布和頻率，再從有限差分時域模擬方法去優化其 Q 值及 V 值。藉由半導體奈米製程，我們成功製作具有極小元件尺寸面積的奈米雷射。透過共焦顯微螢光光譜系統，我們成功地取得並驗證具有極低雷射閾值的單模雷射操作。此外，較小的元件尺寸面積亦造就較佳的力學結構特性，使其非常適合應用於流體環境中的折射率感測器。透過一維光子晶體奈米樑耦合共振腔設計，利用其偶耦合模態集中於耦合結構間隙 (環境介質)的場形分布，以偵測不同濃度的糖水溶液，來實現了其折射率光學感測之功能。

Investigation on One Dimensional Photonic Crystal Nanocavity

on Nanobeam

Student: Li-Hsun Chiu

Advisor: Dr. Po-Tsung Lee

Department of Photonics and Display Institute,
National Chiao Tung University
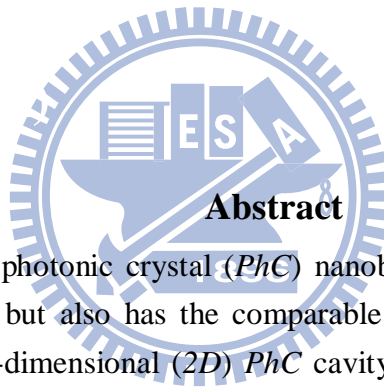
Abstract

One-dimensional (*1D*) photonic crystal (*PhC*) nanobeam (*NB*) cavity not only has the ultra-small device footprint but also has the comparable high quality (*Q*) factor and small mode volume (*V*) with two-dimensional (*2D*) *PhC* cavity. Therefore, *1D PhC NB* cavity is very promising in realizing the application of active nanolasers, optical sensors, and other functional devices in the condensed photonic integrate circuits.

In this thesis, we propose two *1D PhC* nanocavity designs on suspended *NB*, the air-centered and dielectric-centered nanocavities. The optical confinement of nanocavity along the *NB* is provided by multi-hetero-interface with mode-gap effect. From the numerical simulation, finite element method is used for rapidly investigating mode profile and frequency and finite-difference time-domain is used for the *Q* and *V* optimization and. These two nanocavity designs are realized via nano-fabrication processes. By the near-infrared confocal micro-photoluminescence system, single mode lasing actions with low thresholds are achieved and addressed. Moreover, the good mechanical stability due to small device size makes this kind of device suitable for optical sensing. Thus, we propose the *1D PhC* coupled-*NB* nanocavity for optical sensing via utilizing the unique mode distribution of the even mode. Optical sensing function is demonstrated via sensing water glucose water solution with different concentrations.

Acknowledgements

Table of Contents

Table Captions

Chapter 2

Chapter 3

Chapter 4

Figure Captions

Chapter 1

Chapter 2

Chapter 3

Chapter 4

Chapter 1 Introduction

1.1 Photonic Crystal and Defect Devices

In solid physics, the scientists utilize the characteristic of electronic band gap in electronic band structure from the periodic atom arrangement in solid crystal and the propagation of electrons can be manipulated. Actually, the similar manipulation can be achieved in the propagation of photons. In 1987, E. Yablonovitch [1] and S. John [2] firstly propose the concept of "Photonic Crystal" (*PhC*), which is composed of the periodic index variation of different dielectric materials. Photonic band gap (*PBG*) is the unique feature of *PhCs*, which can forbid specific frequency range of light. According to the dimensions of PBG or periodic arrangement, the device can be classified into one- (*1D*), two- (*2D*), and three-dimensional (*3D*) *PhCs*, as shown in Fig. 1-1(a), (b), and (c). Various optical devices can be made by introducing the artificial defects into *PhCs* owing to this *PBG* effect, for example, the point (cavity) and line (waveguide) defects, as shown in Figs. 1-2(a) and (b). Considering the complexity of fabrication process and dimensions of *PBG* effect, *2D* suspended *PhC* with in-plane *PBG* confinement and vertical total-internal-reflection (*TIR*) confinement, as shown in Fig. 1-2(c), would be a good platform to develop various optical devices. A variety of wavelength-scale optical devices have widely developed in the last decade.
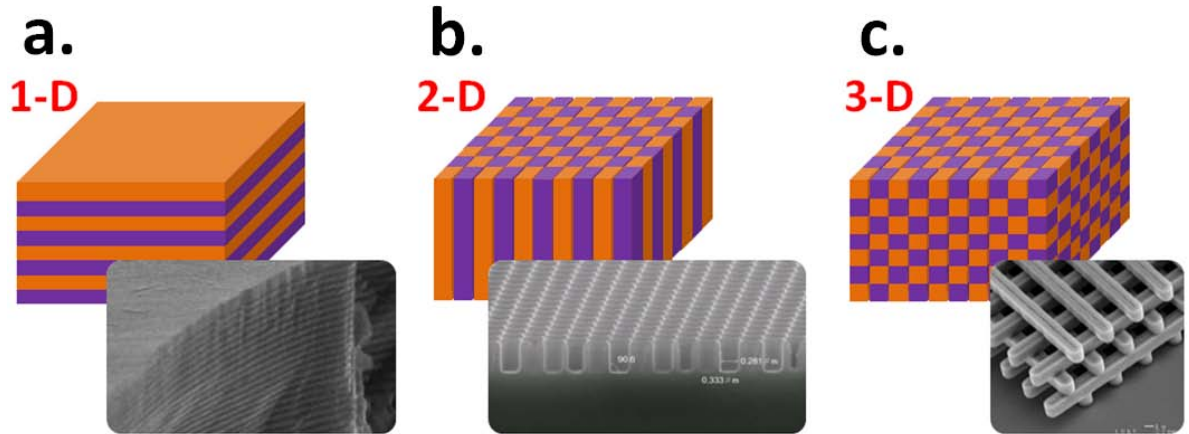
Fig. 1-1: Schemes of (a) *1D* (distributed Bragg reflector), (b) *2D* (periodic air holes on semiconductor material), and (c) *3D PhCs* [3].
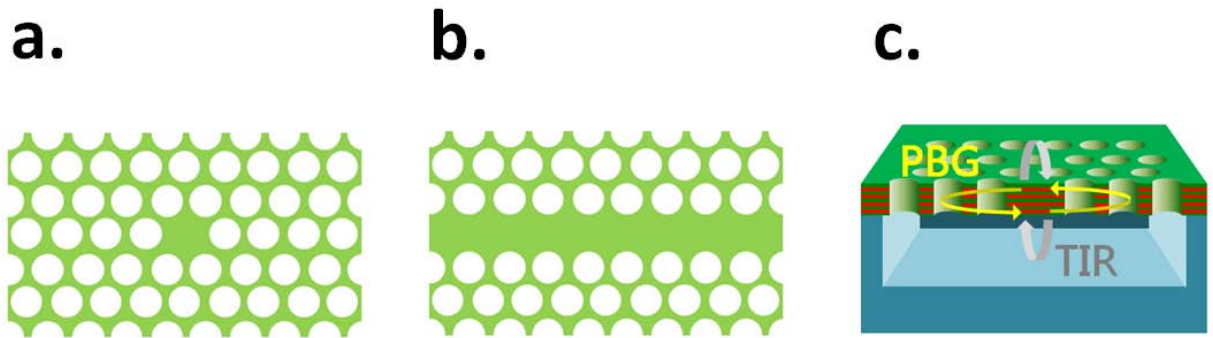
Fig. 1-2: Schemes of the (a) point and (b) line defects for cavity and waveguide based on *2D* triangular lattice *PhCs*. (c) Illustration and confinement mechanism of *2D PhC* nanocavity in a suspended slab.

1.2 *2D PhC* Cavity and its Bottleneck in Footprint Minimization

For constructing a resonant cavity, reflective mirrors play an important role and determine the modal characteristics of resonant modes directly. In the development of *2D PhC* cavity, many scientists have paid great attention on the cavity with high quality (*Q*) factor, small mode volume (*V*), and large *Q/V* value. The *Q* factor shows the capability of a cavity in confining photons, that is, to show how lossy it is. For *2D PhC* cavities, the highest simulated and experimental *Qs* are 5×10^9 [4] and 4×10^6 [5] respectively. In addition, *V* determines the size of mode profile distribution and small *V* has long been regarded as an essential for enhancing light-matter interaction. For a *2D PhC* cavities, the smallest *V* of the mode concentration in slab (n~3.4) is $1.7(\lambda/2n)^3$ by H. S. Ee *et al.* [6]. The resulted ultra-high *Q/V* is beneficial for the strong-coupling phenomenon in cavity quantum electro-dynamics system [7] and the single photon source [8]. Owing to the ultra-high *Q* and ultra-small *V*, *2D PhC* cavity on slab is better than the other optical cavities operating in wavelength-scale. Based on these advantages, it has been widely applied in developing various functional optical devices in photonic integrated circuits (*PICs*), such as low-threshold laser [9, 10], optical sensor [11, 12], optical switches [13], optical buffers [14], channel drop filters [15, 16], and so on. By integrating different functional optical devices, versatile *PICs* on chip will be realized in near future.

In addition to *TIR* effect, the confinement of the *PhC* cavity can be provided by the *PBG* and mode-gap effects. For the confinement provided by the PBG effect, S. Noda *et al.* [17, 18], have reported that one can tune the air hole position around the cavity to efficiently reduce the mode mismatch in the interface of the cavity and the *PhC* mirror, which significantly increases the reflectivity, as shown in Fig. 1-3(a). The reported experimental *Q* (~4.5×10^4) is the highest value in 2003 and its *V* is $0.6(\lambda/n)^3$. However, via the air hole position tuning in *L3* cavity, the electric field distribution cannot be modified to a Gaussian

distribution, as shown in Fig. 1-3(b), and the leakage in the light cone cannot be efficiently suppressed. Therefore, ultra-high Q value cannot be achieved in such design. In 2005, S. Noda *et al.* [19] proposed another *PhC* mirror design based on mode-gap effect, where the electric field is perfectly matching with the Gaussian distribution, as shown in Fig. 1-4(a). Therefore, the vertical loss can be further suppressed. The confinement mechanism of mode-gap effect is utilizing the propagation mode in *2D PhC* waveguide. As shown in Fig. 1-4(b), by tuning the waveguide with lattice a_1 to be a_2, the allowed propagating mode frequency in the waveguide a_2 moves to lower frequency, which cannot propagate in the waveguide a_1. Thus, a_1 / a_2 waveguide interface acts as a mirror and the mode-gap region is formed. Based on this *PhC* mirror design, ultra-high simulated Q of 5×10^8 is achieved.
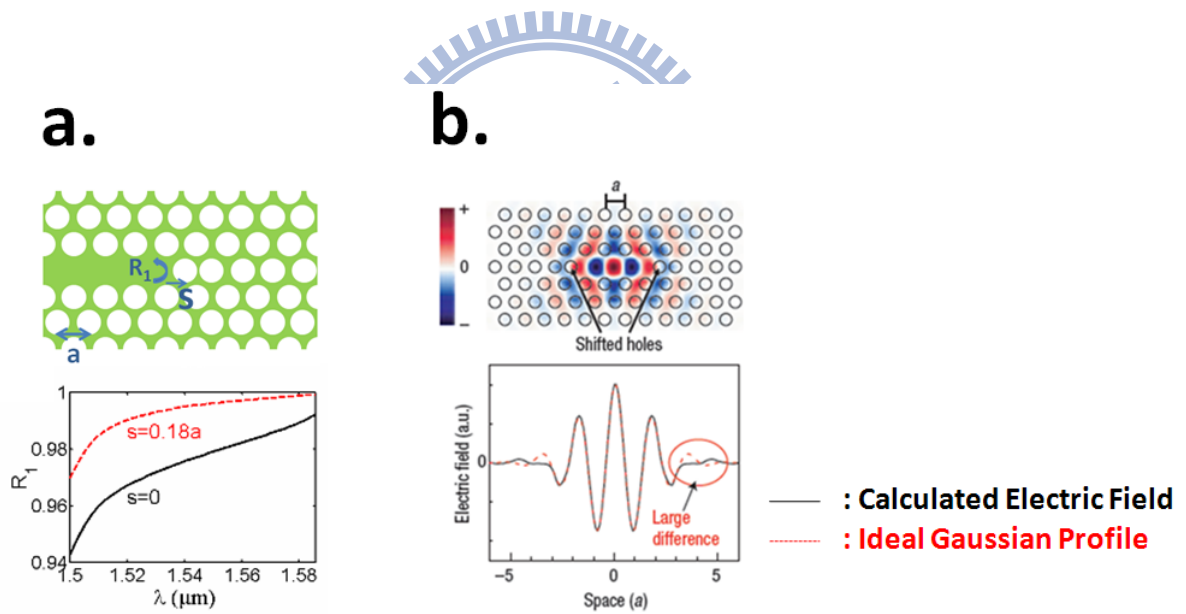
Fig. 1-3: The mirror designs based on the (a) PBG effect with the air-hole shifting to increase the reflectivity of the mirror [17]. (b) Electric field distribution of *2D PhC L3* microcavity with nearest air-hole shifting.
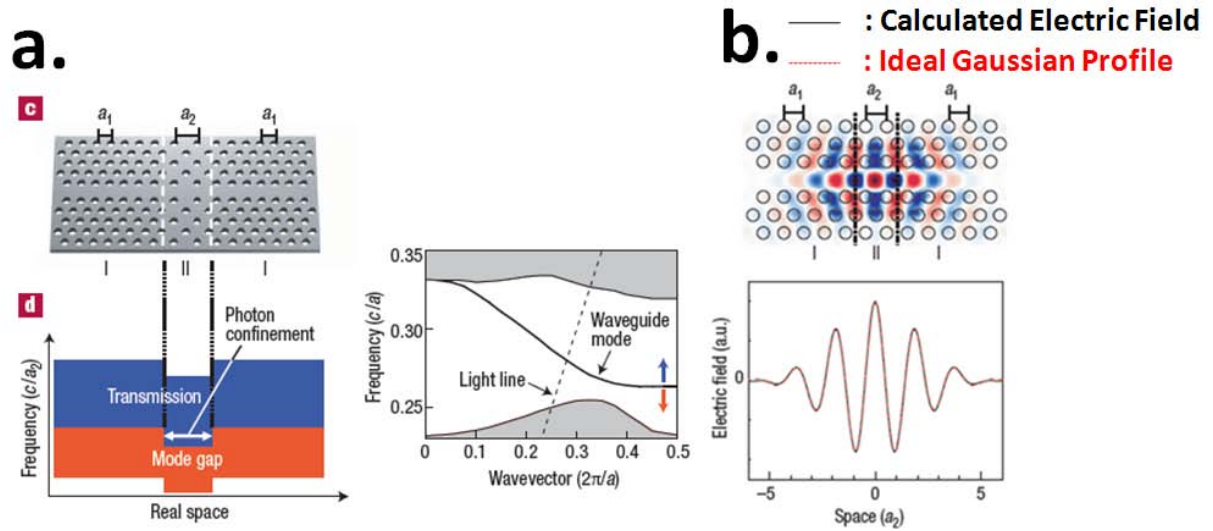
Fig. 1-4: (a) The mirror design based on mode-gap effect via the interface between waveguides with different lattice constant [19]. (b) Electric field distribution of *PhC* nanocavity with mode-gap effect via double hetero-waveguide interface.

To realize the condensed *PICs*, the device footprint minimization is essential, which is a big challenge for the *2D PhC* cavities currently. Take the *PhC* circular-D_2 (CD_2) microcavity [20] for example, over twelve *PhC* periods are needed in the in-plane direction for supporting the great cavity performance. In this case, although the Q achieves 4×10^4, the device footprint is as large as 144 μm^2, as shown in Fig. 1-5(a). Comparing with the microgear [21] with
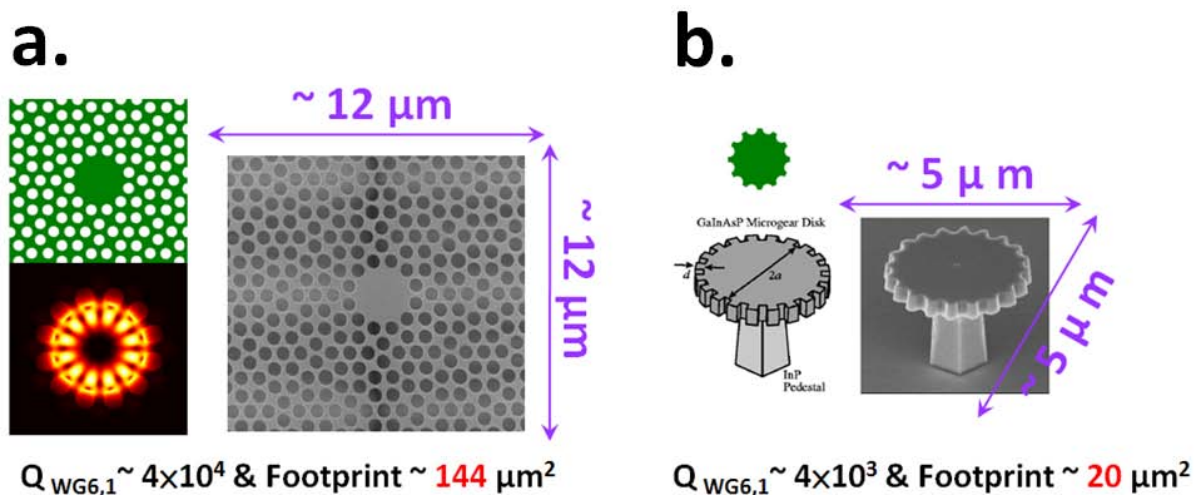
Fig. 1-5: Schemes of (a) *2D PhC CD$_2$* microcavity [20] and (b) microgear microcavity [21].

comparable cavity size, although the Q value of *PhC CD₂* microcavity is one-order higher than that of the microgear, the device footprint of the *PhC CD₂* microcavity is seven times larger than that of the microgear, as shown in Fig1-5(b). Afterward, some scientists tried to shrink the device footprint of *2D PhC* cavity by utilizing its *TIR* confinement mechanism, that is, partially removing the *PhC* periods [22]. However, the shrinkage is limited because further shrinkage in device footprint will greatly reduce the cavity performance.

1.3 *1D PhC* Nanocavity on Nanobeam

Intuitively, replacing one-dimensional *PBG* confinement mechanism by *TIR* effect in *2D PhC* cavity can greatly shrink the device footprint. In 1997, J. S. Foresi *et al.* proposed *1D PhC* nanocavity design on a silicon on insulator (*SOI*) ridge waveguide [23], which is named by *1D PhC* nanobeam (*NB*) nanocavity in the rest of this thesis. In this nanocavity design, the *PBG* and *TIR* effects are used for the confinements along the waveguide and the other two directions respectively, as shown in Fig. 1-5(a). Therefore, the device footprint can be shrunk to 14 μm^2, which makes this structure extremely suitable for integrating in the condensed *PICs*. However, the *Q* value of the *1D PhC NB* nanocavity proposed by Foresi *et al.* is only 2.8 ×10^2. Fortunately, owing to the development of *2D PhC* cavity in the last decade, high *Q 1D PhC NB* has a great breakthrough very recently. In 2008, by using the mode-gap effect, M. Notomi *et al.* proposed a *1D* laddered *PhC* cavity design with continuously gradual hole-spacing modulation, as shown in Fig. 1.5(b), and ultra-high simulated *Q* of 2×10^8 can be achieved [24]. Because this *1D PhC NB* nanocavity design achieve ultra-high *Q* and ultra-small device footprint simultaneously, various *1D PhC NB* nanocavities are widely applied to various optical devices in *PICs*, such as active lasers
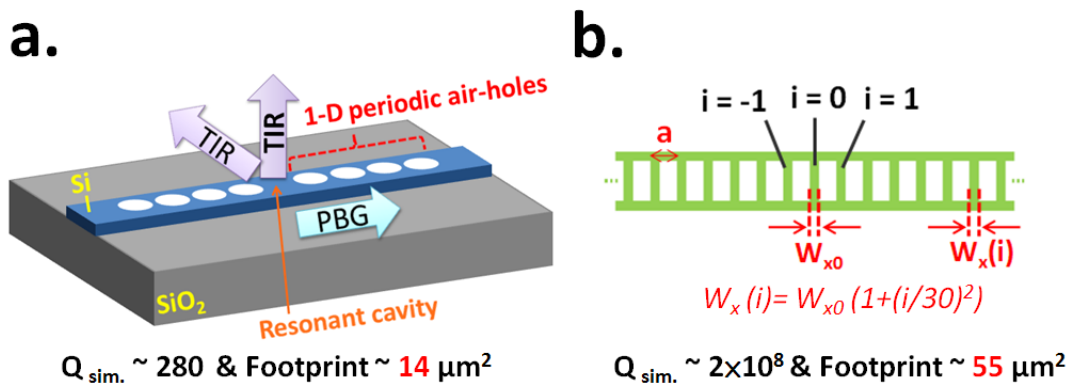
Fig. 1-6: Scheme and confinement mechanisms of (a) *1D PhC NB* nanocavity with four periodic air holes on *SOI* structure [23]. (b) Scheme of *1D* laddered *PhC* cavity with gradual hole-spacing modulation [24].
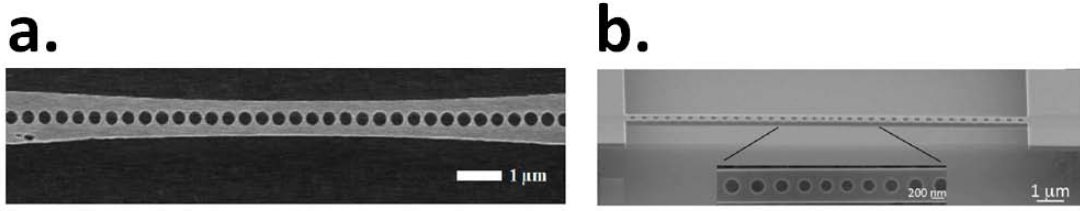
Fig. 1-7: *1D PhC NB* nanocavities with mode-gap effects via (a) beam width modulation [25] and (b) hole-size modulations [27].

[25-30], filters [31-33] ,optical sensors [34], and so on.

Owing to the advantages of the small device footprint, high *Q*, and small V in *1D PhC NB* nanocavity, it is extremely suitable for realizing efficient nanolaser with ultralow lasing threshold in condensed *PICs*. Comparing with the earliest report in *PhC* laser proposed by O. Painter *et al.* [35], it has made a significant progress. A variety of *1D PhC NB* nanocavity lasers have been demonstrated explosively since 2010. Y. H. Lee *et al.* [25] demonstrated *1D* parabolic *NB* laser with mode-gap effect by the continuously gradual modulated beam width, as shown in Fig. 1-6(a). J. Vuckovic *et al.* [26] and M. Loncar *et al.* [27] demonstrated *1D PhC NB* lasers via the *PBG* effect with continuously gradual effective index modulation in quantum dots and wells respectively, as shown in Fig. 1-6(b).   Ultra-low threshold (~19 μW) in Vuckovic's work and high spontaneous emission factor (~0.97) in Loncar's work are successfully achieved. In addition, Y. Halious *et al.* [28, 29] applied the benzo-cyclo-butene bonding technique to integrate the *NB* laser with the waveguide for light leading-out, which is also essential in constructing *PICs*.

In 2010, O. Painter *et al.* [30] proposed *1D* "zipper" cavity laser and the lasing wavelength can be tuned by applying different electrostatic field. This *1D PhC* coupled-*NB* laser design is also applied highly sensitive optical sensor proposed by B. Wang *et al.* [34] due to its unique field distribution and ultra-small line-width. Owing to above developments in various functionalities, constructing versatile and condensed *PICs* via *1D PhC* nanocavities on *NB* becomes foreseeable.

1.4 Motivations and Thesis Overview

For serving as the laser source, *2D PhC* laser cavity based on slab structure has been widely investigated in recent years. However, minimizing the device footprint is still a big challenge. Fortunately, *1D PhC NB* nanocavity can simultaneously achieve high *Q* and small *V* while the device footprint is very small, which is very suitable for being an efficient nanolaser in condensed *PICs* with ultra-high component density.

In this thesis, we design different *1D PhC NB* nanocavities and realized them via semiconductor nano-fabrication process. And then we investigate their properties for serving as the nanolasers and optical sensors. The thesis overview is illustrated as bellow. In chapter 2, we will introduce the methods for designing, fabricating, and characterizing the *1D PhC NB* nanocavity. In chapter 3, two different *1D PhC NB* nanocavities will be introduced and demonstrated via semiconductor laser devices. We will investigate their modal properties both in simulations and experiments. In chapter 4, modal properties of *1D PhC* coupled-*NB* nanocavity will be investigated. And we also investigate the optical sensing abilities of *1D PhC* coupled-*NB* both in simulation and experiment. Finally, in chapter 5, we will summarize our works on *1D PhC NB* nanocavities and future works.

Chapter 2 Numerical Methods, Fabrication Processes and Measurement Setup of *1D PhC NB* Nanocavity Laser

2.1 Introduction

In this chapter, we will introduce the numerical simulations, nano-fabrication processes, and measurement setup for realizing and analyzing the *1D PhC NB* nanocavity lasers. From the numerical simulations, we can obtain photonic band diagram, resonant wavelength, quality factor, and mode volume. To realize the *1D PhC NB* nanocavity based on *InGaAsP* multi-quantum wells (*MQWs*), we have developed the standard nano-fabrication processes. To characterize the devices, we set up a near-infrared (*NIR*) micro-photoluminescence (micro-*PL*) system. The accessories of this system will also be introduced.
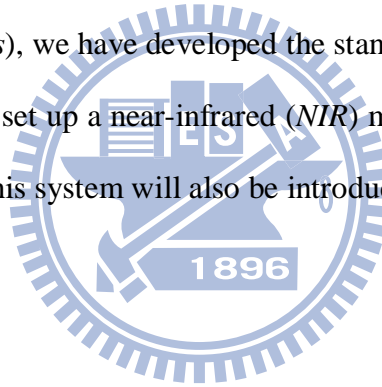
2.2 Numerical Simulation Methods

It is important for us to modal the behavior of photons in various *PhC* structures. In this section, we will introduce several important numerical simulation methods for analyzing the *PhC* devices, including plane-wave expansion (*PWE*), finite-difference time-domain (*FDTD*) methods, and finite-element method (*FEM*).

At first, we need to solve the Maxwell's equations, which are in *MKS* unit and expressed as below:

$$\nabla \cdot \vec{B}(\vec{r}, t) = 0 \tag{2-1}$$

$$\nabla \cdot \vec{D}(\vec{r}, t) = \rho(\vec{r}, t) \tag{2-2}$$

$$\nabla \times \vec{E}(\vec{r}, t) = -\frac{\partial \vec{B}(\vec{r},t)}{\partial t} \tag{2-3}$$

$$\nabla \times \vec{H}(\vec{r}, t) = \vec{J}(\vec{r}, t) + \frac{\partial \vec{D}(\vec{r},t)}{\partial t} \tag{2-4}$$

where the *B*, *D*, *E*, *H*, ρ, and *J* are magnetic flux density, electric displacement, electric fields, magnetic fields, electric charge density, and electric current density respectively. There are several assumptions: (1) The dielectric material is isotropic, lossless, and non-magnetic. Thus, $\vec{D}(\vec{r}, t)$ and $\vec{B}(\vec{r}, t)$ can be written as $\varepsilon_0 \varepsilon(\vec{r}) \vec{E}(\vec{r}, t)$ and $\mu_0 \vec{H}(\vec{r}, t)$, where ε_0 and μ_0 are permittivity and permeability in free space and the term of $\varepsilon(\vec{r})$ is determined by the different periodic structures. In addition, $\varepsilon(\vec{r})$ would be a real value. (2) There is no free charge in space, which makes $\vec{J}(\vec{r}, t)$ and $\rho(\vec{r}, t)$ both equal to zero. Under these assumptions, the equations (2-1) – (2-4) can be simply rewritten as the following:

$$\nabla \cdot \vec{H}(\vec{r}, t) = 0 \tag{2-5}$$

$$\nabla \cdot \varepsilon(\vec{r}) \vec{E}(\vec{r}, t) = 0 \tag{2-6}$$

$$\nabla \times \vec{E}(\vec{r}, t) = -\mu_0 \frac{\partial \vec{H}(\vec{r},t)}{\partial t} \tag{2-7}$$

$$\nabla \times \vec{H}(\vec{r}, t) = \varepsilon_0 \varepsilon(\vec{r}) \frac{\partial \vec{E}(\vec{r},t)}{\partial t} \tag{2-8}$$

The solutions in electric and magnetic fields are the harmonic functions and the solutions can be written as the product of spatial and time functions by applying the separation of variables. The terms of $\vec{E}(\vec{r}, t)$ and $\vec{H}(\vec{r}, t)$ can be written as the following forms:

$$\vec{H}(\vec{r}, t) = \vec{H}(\vec{r}) e^{i\omega t} \tag{2-9}$$

$$\vec{E}(\vec{r}, t) = \vec{E}(\vec{r}) e^{i\omega t} \tag{2-10}$$

We can obtain the master equation for magnetic field and the wave equation for electric field by substituting (2-9)- (2-10) into (2-7) - (2-8), as shown in the following:

$$\nabla \times \left(\frac{1}{\varepsilon(\vec{r})} \nabla \times \vec{H}(\vec{r}) \right) = \frac{\omega^2}{c_0^2} \vec{H}(\vec{r}) = k_0^2 \vec{H}(\vec{r}) \qquad \text{(2-11) Master equation}$$

$$\nabla \times (\nabla \times \vec{E}(\vec{r})) = \frac{\omega^2}{c_0^2} \varepsilon(\vec{r}) \vec{E}(\vec{r}) = k_0^2 \varepsilon(\vec{r}) \vec{E}(\vec{r}) \qquad \text{(2-12) Wave equation}$$

where c_0 is the velocity of light wave in vacuum and k_0 is the wavevector in reciprocal space. Thus, for a given *PhC* structure, we can solve (2-11) and (2-12) to obtain the modes $\vec{H}(\vec{r})$ and $\vec{E}(\vec{r})$ at certain frequency.
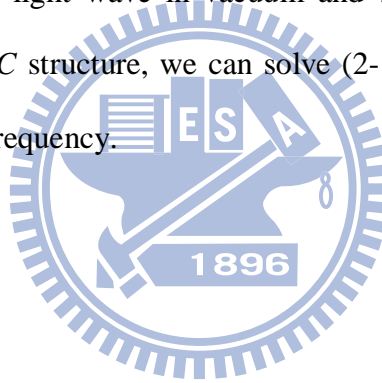
2.2.1 Plane-Wave Expansion Method

Plane-wave expansion method (*PWE*) is a convenient method to calculate the band diagram for a given *PhC* structure. The calculation begins from expanding dielectric function and periodic part of the Bloch function into the Fourier series expansion in reciprocal lattice vectors ($\vec{G}$). Then we obtain the following equations:

$$\varepsilon(\vec{r}) = \sum_{\vec{G}} \varepsilon_{\vec{G}} \, e^{i\vec{G}\cdot\vec{r}} \tag{2-13}$$

$$\vec{H}(\vec{r}) = \sum_{\vec{G}} h_k(\vec{G}) \, e^{i(\vec{G}+\vec{k})\cdot\vec{r}} \tag{2-14}$$

where the Fourier coefficient, $\varepsilon_{\vec{G}} = \frac{1}{V_c} \int_{\text{unit cell}} e^{-i\vec{G}\cdot\vec{r}} \, \varepsilon(\vec{r})$ and V_c is the volume of the unit cell. Once the amplitude of $\vec{H}(\vec{r})$ [$h_k(\vec{G})$] of the plane wave is determined, we will obtain the solution of $\vec{H}(\vec{r})$ of equation (2-11). By substituting equation (2-13) and (2-14) into the master equation (2-11), the master equation becomes:

$$\left(\vec{k} + \vec{G}\right) \sum_{\vec{G}'} \varepsilon_{\vec{G}-\vec{G}'}^{-1} \left(\vec{k} + \vec{G}'\right) h_k(\vec{G}') = -\frac{\omega^2}{c_0^2} h_k(\vec{G}') \tag{2-15}$$

Equation (2-15) is a $2N \times 2N$ matrix form and N is the numbers of plane wave applied in calculation. By matrix diagonalization methods, we can solve this equation and the dispersion curve of *PhC* device is obtained. The $\varepsilon_{\vec{G}-\vec{G}'}$ is the Fourier coefficient of $\varepsilon(\vec{r})$ relating to the reciprocal lattice constant, $\vec{G} - \vec{G}'$ and $\vec{k}$ is the wavevector in first Brillouin zone. In this thesis, the band diagrams are all calculated via *PWE* method.

2.2.2 Finite-Difference Time-Domain Method

In nowadays, finite-difference time-domain (*FDTD*) method is a popular way to model the behaviors of electro-magnetic wave in the different structures and materials. Its unique characteristic different from *PWE* methods is the ability of directly solving the time-dependent Maxwell's equations. Furthermore, *FDTD* method is a spatial grid-based method. Thus, we illustrate this methods by writing the equations (2-6) and (2-7) in Cartesian coordinates and discretizing the partial derivatives of spatial and time domain with the utilization of central-difference approximations.

Six scalar equations of equations (2-6) and (2-7) in the free-charge space:

[In isotropic, lossless, and non-magnetic materials]

$$\frac{\partial E_x}{\partial t} = \frac{1}{\varepsilon_0 \varepsilon(\vec{r})}\left(\frac{\partial H_z}{\partial y} - \frac{\partial H_y}{\partial z}\right) \tag{2-16}$$

$$\frac{\partial H_x}{\partial t} = \frac{1}{\mu_0}\left(\frac{\partial E_y}{\partial z} - \frac{\partial E_z}{\partial y}\right) \tag{2-17}$$

$$\frac{\partial E_y}{\partial t} = \frac{1}{\varepsilon_0 \varepsilon(\vec{r})}\left(\frac{\partial H_x}{\partial z} - \frac{\partial H_z}{\partial x}\right) \tag{2-18}$$

$$\frac{\partial H_y}{\partial t} = \frac{1}{\mu_0}\left(\frac{\partial E_z}{\partial x} - \frac{\partial E_x}{\partial z}\right) \tag{2-19}$$

$$\frac{\partial E_z}{\partial t} = \frac{1}{\varepsilon_0 \varepsilon(\vec{r})}\left(\frac{\partial H_y}{\partial x} - \frac{\partial H_x}{\partial y}\right) \tag{2-20}$$

$$\frac{\partial H_z}{\partial t} = \frac{1}{\mu_0}\left(\frac{\partial E_x}{\partial y} - \frac{\partial E_y}{\partial x}\right) \tag{2-21}$$

In 1966, K. Yee [35] described the basis of *FDTD* method for electro-magnetic wave with gridded space domain and stepped time domain. In spatial domain, Yee proposed the concept of "Yee cell", as shown in Fig 2.1(a). Within this cell, all the $\vec{E}$ ($\vec{H}$) components are surrounded by four $\vec{H}$ ($\vec{E}$) components. It means that we can obtain $\vec{E}$ components if their corresponding $\vec{H}$ components are known, and vice versa. In time domain, Yee proposed the "leapfrog scheme", as shown in Fig 2.1(b). Within this scheme, $\vec{E}$ and $\vec{H}$ fields would be updated by each other under the proceeding time step. In other words, $\vec{E}$ field within the Yee

cell would be calculated at a given time-step and then $\vec{H}$ field within the same Yee cell would be calculated at the next time-step. This calculation is processed under the discretization of equations (2-16) - (2-21), as described by equations (2-22) and (2-23):

$$E_x|_{i+\frac{1}{2},j,k}^{n+1} = E_x|_{i+\frac{1}{2},j,k}^{n} + \frac{\Delta t}{\varepsilon_0 \varepsilon(\vec{r})\Delta y}\left(H_z|_{i+\frac{1}{2},j+\frac{1}{2},k}^{n+\frac{1}{2}} - H_z|_{i+\frac{1}{2},j-\frac{1}{2},k}^{n+\frac{1}{2}}\right) - \frac{\Delta t}{\varepsilon_0 \varepsilon(\vec{r})\Delta z}\left(H_y|_{i+\frac{1}{2},j,k+\frac{1}{2}}^{n+\frac{1}{2}} - H_y|_{i+\frac{1}{2},j,k-\frac{1}{2}}^{n+\frac{1}{2}}\right)$$

(2-22)

$$H_x|_{i,j+\frac{1}{2},k+\frac{1}{2}}^{n+\frac{1}{2}} = H_x|_{i,j+\frac{1}{2},k+\frac{1}{2}}^{n-\frac{1}{2}} + \frac{\Delta t}{\mu_0 \Delta z}\left(E_y|_{i,j+\frac{1}{2},k+1}^{n} - E_y|_{i,j+\frac{1}{2},k}^{n}\right) - \frac{\Delta t}{\mu_0 \Delta y}\left(E_z|_{i,j+1,k+\frac{1}{2}}^{n} - E_z|_{i,j,k}^{n}\right)$$

(2-23)

where Δx, Δy, Δz are the grid size and Δt is the time step. Supposed that $F(x, y, z, t)$ is either one of the $\vec{E}$ and $\vec{H}$ fields, $F(x, y, z, t)$ can be written as $F(i\Delta x, j\Delta y, k\Delta z, n\Delta t) \equiv F|_{i,j,k}^{n}$ under the spatial and temporal discretization. Thus, the index i, j, k, n represent the grid points of position and time. Here we only show the discretization form of E_x and H_x components. Likewise, the discretization form of E_y, E_z, H_y, and H_z can be treated in the same way.

Via the numerous and repetitive above-processes, the desired electro-magnetic field can be resolved. Therefore, we can investigate the characteristics of *1D PhC NB* nanocavity structure in this thesis.
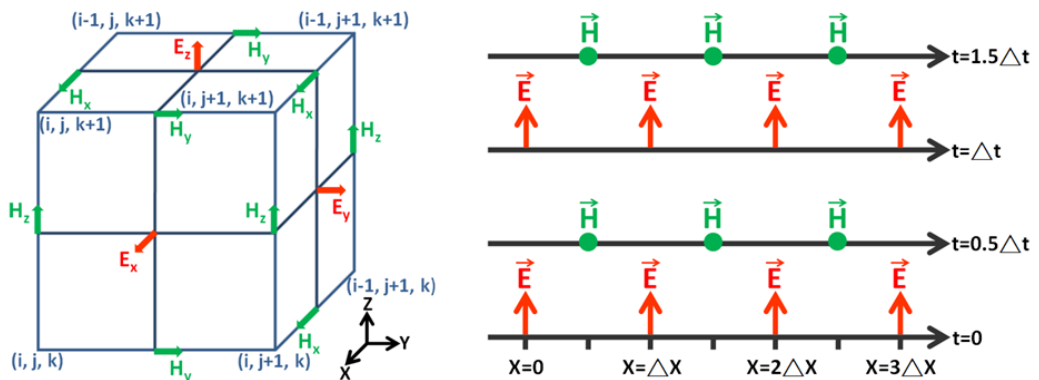
Fig. 2-1: (a) Yee cell: Illustration of the spatial discretization in *FDTD* algorism. (b) Space-time chart in *FDTD* algorism: centeral differences for space derivatives and leapfrog scheme for time derivatives.

2.2.3 Finite-Element Method

Finite-Element Method (*FEM*) is a promising method for solving partial differential equations (*PDEs*), for example, equations (2-11) and (2-12) in electromagnetic. In addition to the modeling of electromagnetic wave, it is also powerful in solving the *PDEs* in heat transfer fluid mechanics and mechanical systems. In order to obtain the solution of wave equation in general form together with the appropriate boundary conditions, standard *FEM* proceeds in three steps [36].

First, via the variational method, we obtain the function of the wave equation for electric fields and the calculation is proceeding under the source-free surroundings. After simplification, the function becomes:

$$F = \frac{1}{2} \int_{\Omega} [\frac{1}{\mu_r} (\nabla \times \vec{E}) \cdot (\nabla \times \vec{E}) - k_0^2 \varepsilon_r \vec{E} \cdot \vec{E}] d \tag{2-24}$$

where μ_r and ϵ_r are the relative permeability and permittivity of material, Ω is the computational domain of a given structure. Then the second and most demanding step of *FEM* is the discretization in spatial domain and the number of mesh elements will strongly affect the computation time and the accuracy of the numerical results. In addition, the mesh elements is tetrahedral [shown in Fig 2.2] and it can construct the geometry of *PhCs* very well. Third, we have to find out the interpolation function and then we can obtain the approximation solution of unknown electric filed within an element. Under the linear approximation of electric fields in each mesh elements ($\vec{E}^e = a + bx + cy + dz$), it can be expressed as the following equation after summarization:

$$\vec{E}^e = \sum_{i=1}^{4} \vec{N}_i^e (x,y,z) \, E_i^e = \{E_i^e\}^T \{\vec{N}^e\} = \{\vec{N}^e\}^T \{E_i^e\} \tag{2-25}$$

$$[\vec{N}_i^e (x,y,z) = \frac{1}{6V^e} (a + bx + cy + dz), V^e \text{ is the volume of the element}]$$

where e and i denote as the element numbers and node numbers in a mesh element. For example, $\vec{E}_i^e$ is the electric field at the i-th node of a mesh element. $\vec{N}_i^e (x,y,z)$ is the

interpolation function which can be determined by implanting four nodes in a mesh element into the linear approximation form. Finally, on substituting equation (2-25) into (2-24), we obtain

$$F = \frac{1}{2}\sum_{e=1}^{M}\{\vec{E}^e\}^T[A^e]\{E^e\} - k_0{}^2\{\vec{E}^e\}^T[B^e]\{E^e\} \tag{2-26}$$

where

$$[A^e] = \int_{\Omega^e}\frac{1}{\mu_r^e}\{\nabla \times \vec{N}^e\} \cdot \{\nabla \times \vec{N}^e\}^T \, dV \ ,$$

$$[B^e] = \int_{\Omega^e}\varepsilon_r^e\vec{E} \cdot \vec{E} \, dV,$$

Ω_e is the computational domain within the mesh element, and M is the total number of elements. After carrying out the summation, equation (2-26) can be written as

$$F = \frac{1}{2}(\{E\}^T[A]\{E\} - k_0{}^2\{E\}^T[B]\{E\}) \tag{2-27}$$

By applying $\delta F = 0$, the eigenvalue system is obtained as the following.

$$[A]\{E\} = k_0{}^2[B]\{E\} \tag{2-28}$$

We can solve equation (2-28) by imposing the Dirichlet boundary condition to zero out the edge fields coincident with the cavity wall. Once the $\{E\}$ and its eigenfrequency are solved, we can compute the desired parameters, such as the scattering or radiation pattern, and displaying the result in the form of curves, plots, or color pictures. Therefore, we utilize *FEM* to obtain the eigenfrequency and mode profile of the desired *PhC* structure in this thesis.
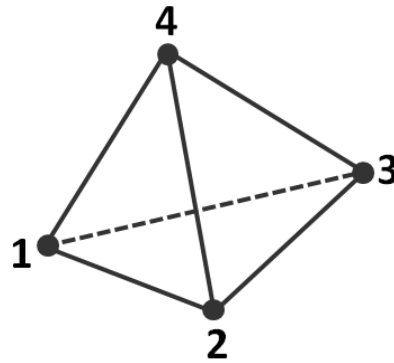
Fig. 2-2: Scheme of the tetrahedral mesh element.

2.3 Nano-Fabrication Process of *PhC* Slab

To fabricate the desired *PhC* devices, *InGaAsP* multi-quantum wells (*MQWs*) epitaxial structure on *InP* substrate is prepared, as shown in Table 2-1, which is grown by metal-organic chemical vapor deposition (*MOCVD*). The *MQWs* are consisted of four 10 nm compressively-strained (*CS*) *InGaAsP* wells ($\lambda_{bandgap}\sim 1.55$ μm), which are separated by five 15 nm tensile-strained (*TS*) *InGaAsP* barriers ($\lambda_{bandgap}\sim 1.25$ μm). The total thickness of *InGaAsP MQWs* is about 225 nm and its photoluminescence (*PL*) spectrum is centered at 1.55 μm.

Table 2-1: *InGaAsP MQWs* epitaxial structure on *InP* substrate, which is grown by Land Mark Optoelectronic *Inc.*, Taiwan.

Layer Name		Description	Thickness	$\lambda_{bandgap}$
Tensile-Strained InGaAsP		Upper SCH layer	55 nm	1.25 μm
Tensile-Strained InGaAsP		Barrier(-0.2%~0.3% TS)	15 nm	1.25 μm
Compressively-Strained InGaAsP	4 pairs	Well(0.5%~0.7% CS)	10 nm	1.55 μm
Tensile-Strained InGaAsP		Barrier(-0.2%~0.3% TS)	15 nm	1.25 μm
Tensile-Strained InGaAsP		Lower SCH layer	55 nm	1.25 μm
InP		Buffer layer	500 nm	
InP		N-type substrate		

2.3.1 Overview of the Fabrication Processes

At first, we show the nano-fabrication flow chart of *PhC* slab, as shown in Fig 2-3. The details of each step are illustrated in the following sections.
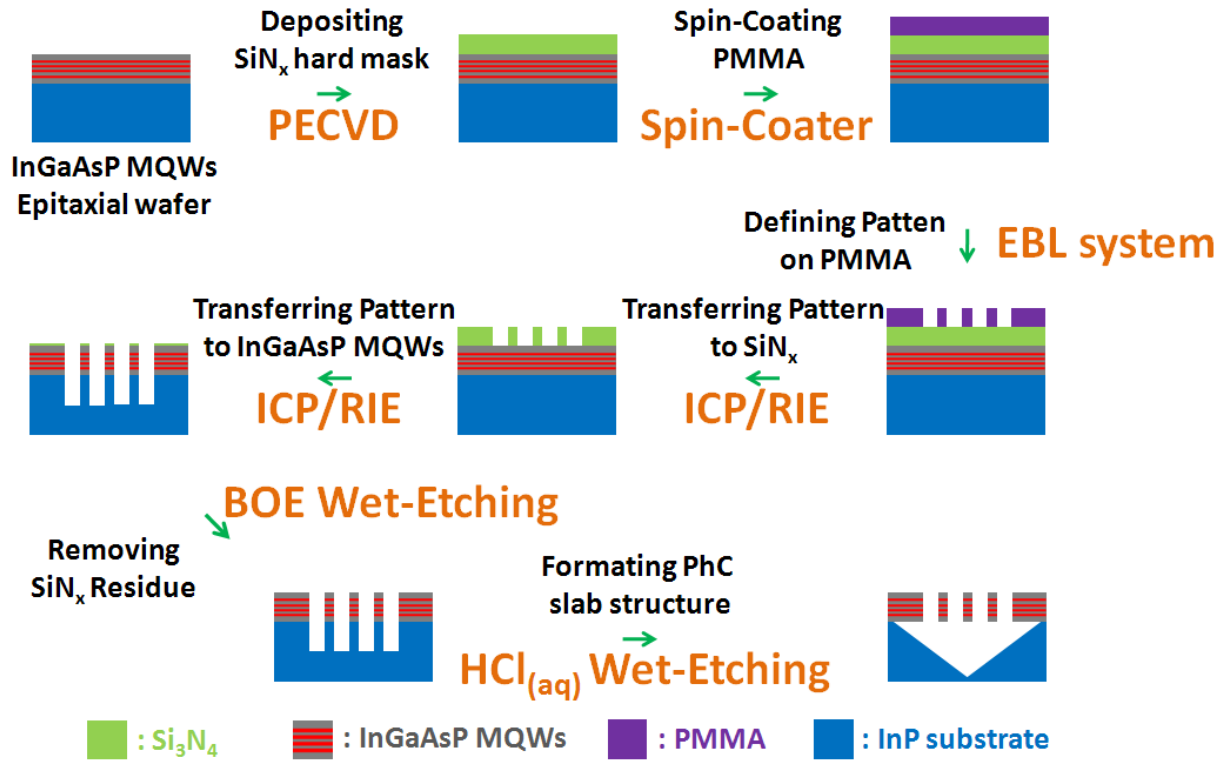
Fig. 2-3: Nano-fabrication flow chart of *PhC* slab structure.

2.3.2 SiN_x Hard Mask Deposition

At first, we deposit a 200 nm SiN_x layer on the epitaxial wafer plasma-enhanced chemical vapor deposition (*PECVD*) by Oxford Instruments Plasma Technology Plasmalab 80 Plus, as shown in Fig 2.3. The SiN_x layer is served as the hard mask for the following selective dry-etching process. The SiH_4 / NH_3 / N_2 mixed gas with flow rate of SiH_4 / NH_3 / N_2 is 8 *sccm* / 8 *sccm* / 250 *sccm* is used at chamber temperature of 200 ℃, pressure of 1000 mTorr, and 20 W *RF* power. The deposition rate of SiN_x under this condition is about 38 nm/min. In addition, the quality of the SiN_x film controlled by the ratio of SiH_4 / NH_3 / N_2 is optimized, which guarantee that we can remove the SiN_x residue by buffer-oxide-etchant (*BOE*) wet-rtching after the dry-etching processes.

Fig. 2-4: Picture of *PECVD* system (Oxford Instruments Plasma Technology Plasmalab 80 Plus), facilities of Center for Nano-Science and Technology (*CNST*), National Chiao Tung University (*NCTU*).

2.3.3 Electron-Beam Lithography for Defining Patterns

Then we use the ELS - 7500EX electron beam lithography (*EBL*) system shown in Fig 2-4 for defining the *PhC* pattern. In this process, there are three steps. First, a 240 nm positive resist, poly-merthyl methacrylate (*PMMA*), is spin-coated on the *MQWs* with *SiN$_x$* mask by a spin-coater. Second, the *PhC* pattern is defined on the *PMMA*-coated sample according to our computer-aided design (*CAD*) via the *EBL* system. Several dosages of electron beam are applied to include suitable dosage for the desired parameters of the *PhCs*. The beam position resolution of ELS-7500EX is 0.625 nm under the $150 \times 150\mu m$ writing field. Third, written *PhC* patterns on *PMMA* are developed and fixed by immersing in the methyl-isobutyl ketone (*MIBK*) and iso-propyl alcohol (*IPA*) solution at 24~25 ℃ in sequence. Then, the pattern on *PMMA* can be served as the first mask for the following dry-etching processes.

Fig. 2-5: *EBL* system (ELS - 7500EX), facilities of *CNST*, *NCTU*.

2.3.4　Dry Etching Processes for Transferring *PhC* Patterns

The following dry etching procedures for transferring pattern into the SiN_x hard mask and *MQWs* are done by the inductively-coupled plasma reactive-ion etching (*ICP-RIE*), Oxford Instruments Plasma Technology Plasmalab 100 shown in Fig 2-5(a). In this process, there are two dry-etching steps. The first dry etching process transfers the patterns from the *PMMA* to SiN_x hard mask. The CHF_3 / O_2 mixed gas with the flow rate of CHF_3 / O_2 is 50 sccm / 5 sccm is used at chamber temperature of 20 ℃, pressure of 55 mTorr, and 150 W *RF* power. The etching rate of SiN_x under this condition is about 80 nm/min. The second dry etching process then transfers the patterns from the SiN_x hard mask to *InGaAsP* / *InP*. The Cl_2 / H_2 / CH_4 mixed gas with flow rate of 6.5 *sccm* / 13.5 *sccm* / 11.5 *sccm* is used at chamber temperature of 150 ℃, pressure of 4 mTorr, and 85 W / 1000 W *RF* power / *ICP* power. The etching rate of *InP* / *InGaAsP* under this condition is about 440 nm/min and the etching selectivity ratio to SiN_x is 4. Scanning electron microscope (*SEM*) picture of the cross-section of the *PhCs* on *InGaAsP MQWs* is shown in Fig. 2-5(b), where the sidewall angle is about 86° - 87°.
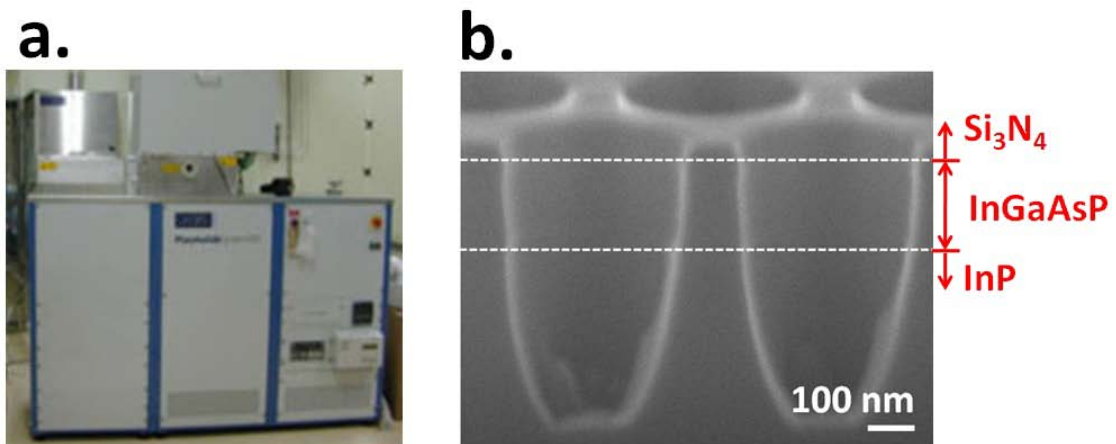
Fig. 2-6: *ICP-RIE* system (Oxford Instruments Plasma Technology Plasmalab 100), facilities of *CNST*, *NCTU*. (b) *SEM* picture of cross-section of the *PhCs* after a series of dry etching processes.

2.3.5   Wet Etching for Suspended Slab Structure Formation

Then the dry-etching processes are followed by the *BOE* and *HCl* selective wet-etching. The former one is used to remove the *SiN$_x$* residue and the latter one is used to form the suspended slab structure via removing the *InP* below the *InGaAsP MQWs*. According to the selective wet-etching chemistry [37], the solution of *HCl* : H_2O = 3 : 1 at 2 ℃ is applied to form the suspended *InGaAsP MQWs* slab and smooth the *InGaAsP* slab surface.
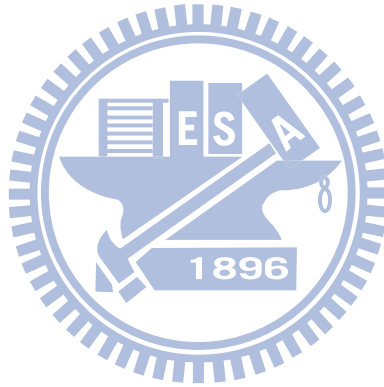
2.4 Measurement Setup

To characterize the *PhC* lasers and emitters, a near-infrared (*NIR*) confocal mico-photoluminescence (micro-*PL*) is setup, as shown in Figs. 2-7 and 2-8.

In this system, a 845 nm transistor-transistor logic (*TTL*) diode laser (Power Technology *Inc.*, APMT-60) is served as the pump source. To operate in the pulsed mode, a function generator (Stanford *Inc.*, DG-535) is connected to a *DC* power source for modulating the output driving current. From this function generator, the pulse width and duty cycle of output signal are set to 15 ns and 100 kHz. The pump laser beam is split into two beams via a 50 / 50 beam splitter (*BS*), it. One beam will be reflected into a 100X long working distance *NIR* objective lens with numerical aperture of 0.42 and then focused on the sample. Another beam will transmit the *BS* to the power meter (Newport *Inc.*, 1815-C). By reading the power value shown in the power meter, the incident power can be estimated.

To precisely pump the cavity region of our devices, a microscope system with a white light source and a charge-couple device (*CCD*) camera is setup in the micro-*PL* system. In addition, the sample is mounted on an 3-axes piezo-stage with minimum moving step of 30 nm and the efficient pumping on the cavity can be achieved via the microscope system.

Once the cavity is pumped, the emission will be collected via the 100X objective lens. A both-side polished Si wafer is placed in front of the receiving end to block the reflected pump source. Then the emission is feed into a multimode fiber (*MMF*) via a 10X objective lens. The *MMF* is connected into optical spectrum analyzer (*OSA*) (Ando *Inc.*, AQ-6315A) and *InGaAs* power meter (Advantest *Inc.*, Q8221) to analyze the emission properties.
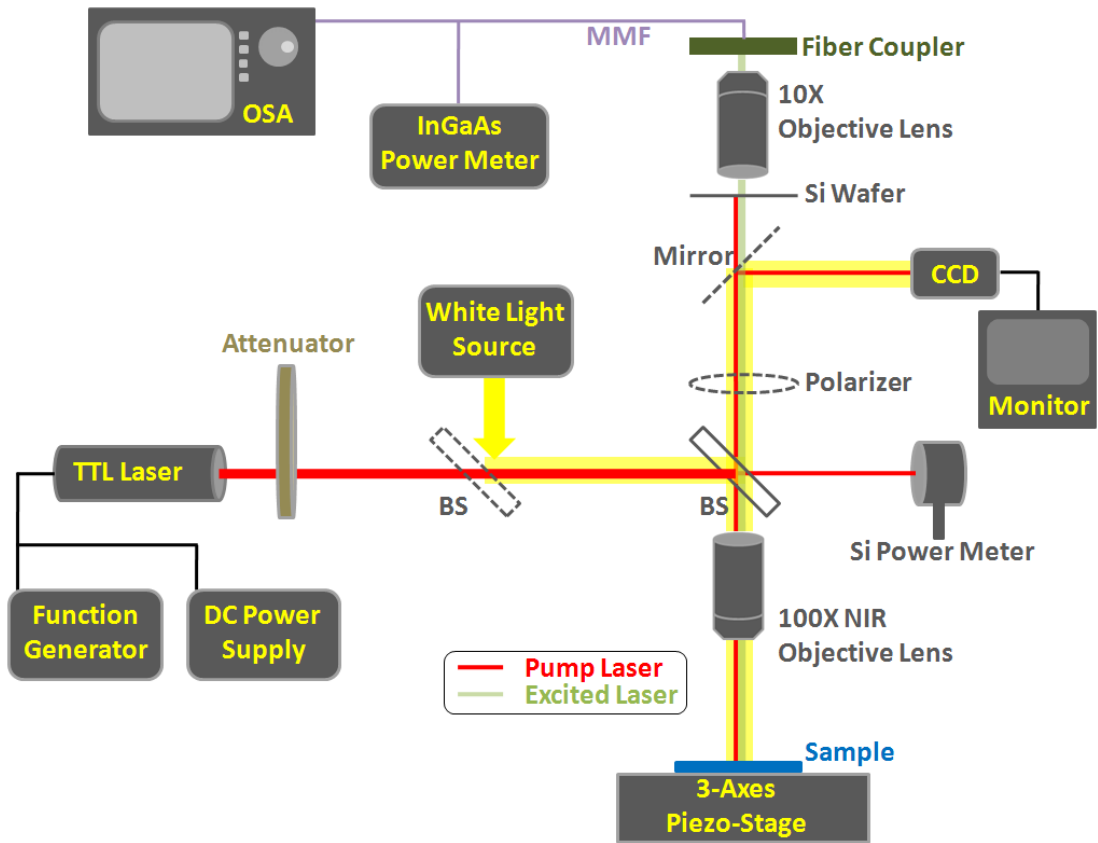
Fig. 2-7: Configuration of the *NIR* confocal micro-*PL* system.
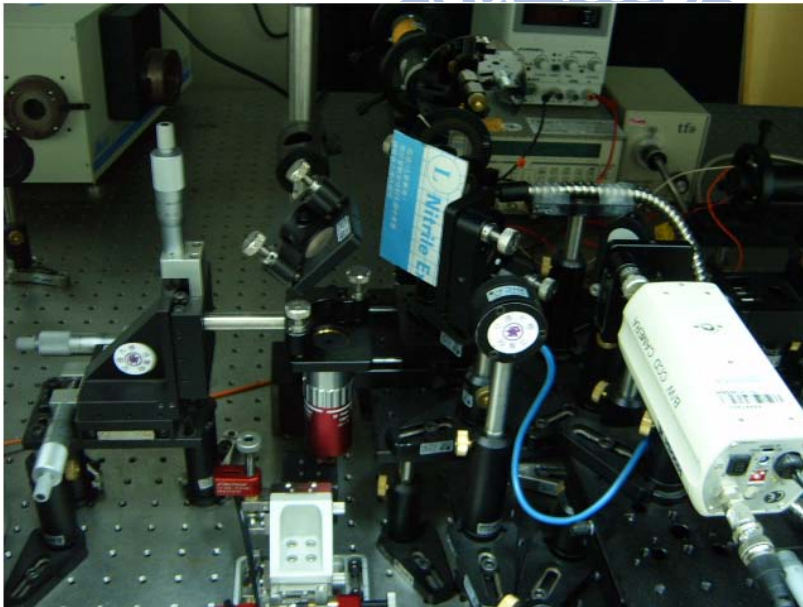
Fig. 2-8: Picture of the *NIR* confocal micro-*PL* system.

2.5 Summary

In this chapter, we have described the theories of numerical methods used for analyzing the *PhC* structures, including *PWE*, *FDTD*, and *FEM*. Subsequently, the nano-fabrication process for *PhC* slab structure based on InGaAsP *MQWs* are introduced, including the techniques of *PECVD* deposition, *EBL* system, *ICP-RIE* dry etching, and selective wet etching. Finally, we setup a *NIR* con-focal micro-*PL* system to characterize the emission properties of the *PhC* devices.
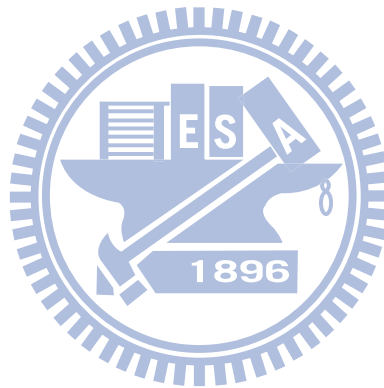
Chapter 3 *1D PhC* Nanocavities on Nanbeam

3.1 Introduction

In this chapter, at first, we will introduce two different one-dimensional (*1D*) photonic crystal (*PhC*) nanobeam (*NB*) nanocavity designs. Via numerical simulations, we will investigate the characteristics of defect modes in *1D PhC NB* nanocavities and the structure will be optimized for large quality (*Q*) factor and small mode volume (*V*), that is high *Q/V*. For serving as an active laser, these nanocavity designs with all-gradual *PhC* mirror are fabricated on *InGaAsP* multi-quantum-wells (*MQWs*) suspended slab structure. The measurement results will be addressed by *FDTD* and *FEM* simulation. Finally, we will summarize our work on *1D PhC NB* nanocavities.
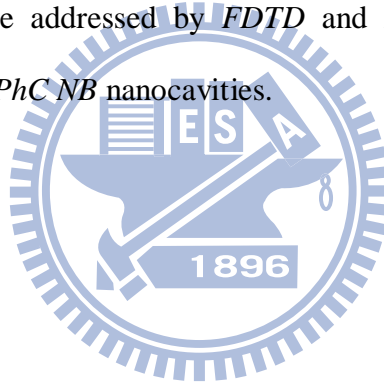
3.2 Design of *1D PhC* Nanocavity on Nanobeam

We design two different *1D PhC NB* nanocavities on suspended nanobeam (*NB*), the air-centered and the dielectric-centered nanocavities, whose center region is air-hole and vein (dielectric region between air holes) respectively, as shown in Fig. 3-1.

The width (*w*), thickness (*t*), and refractive index (n_{NB}) of the *NB* are 600 nm, 220 nm, and 3.4 respectively. The air-hole radius of *1D PhC* is fixed at 126nm. To form the *1D PhC* mirror with mode-gap effect, the lattice constant (*a*) increases digitally from 360 m (a_c) with 5 nm increment (*Δa*) away from the cavity, as shown in Fig. 3-2(a). The mode-gap effect via tuning lattice constant is illustrated by the band diagrams of *1D PhC* on *NBs* with a_1 and a_2 ($a_2 > a_1$) in Fig. 3-2(b). For *1D PhCs* with a_1 and a_2 on *NB*, the propagating mode frequency in a_1 is higher than a_2, which means the mode propagates in a_1 will be forbidden in a_2 and the *1D PhC* with a_2 acts like a mirror. To further reduce the optical scattering losses, multi-hetero-interface with mode-gap effect is usually applied, for example, digitally tuning the lattice constant shown in Fig. 3-2(a).
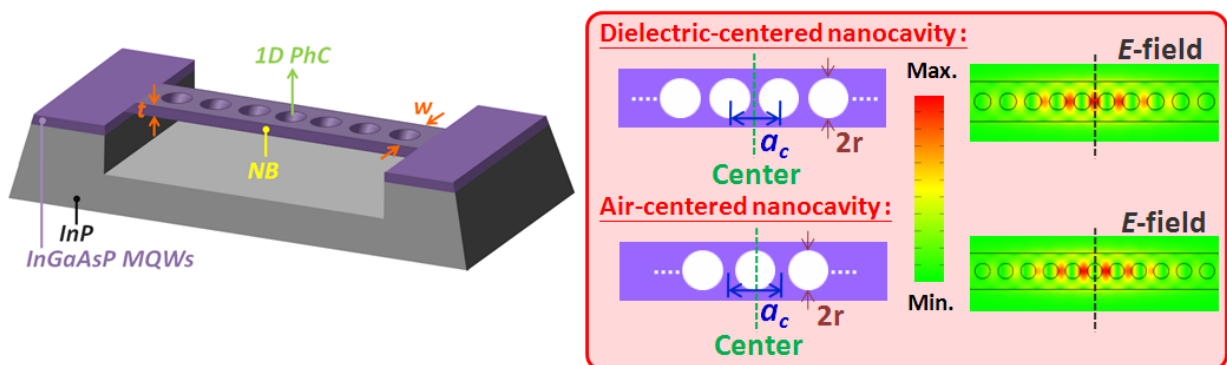
Fig. 3-1: Dielectric- and air-centered *1D PhC NB* nanocavities on a suspended *InGaAsP MQWs* suspended slab structure.
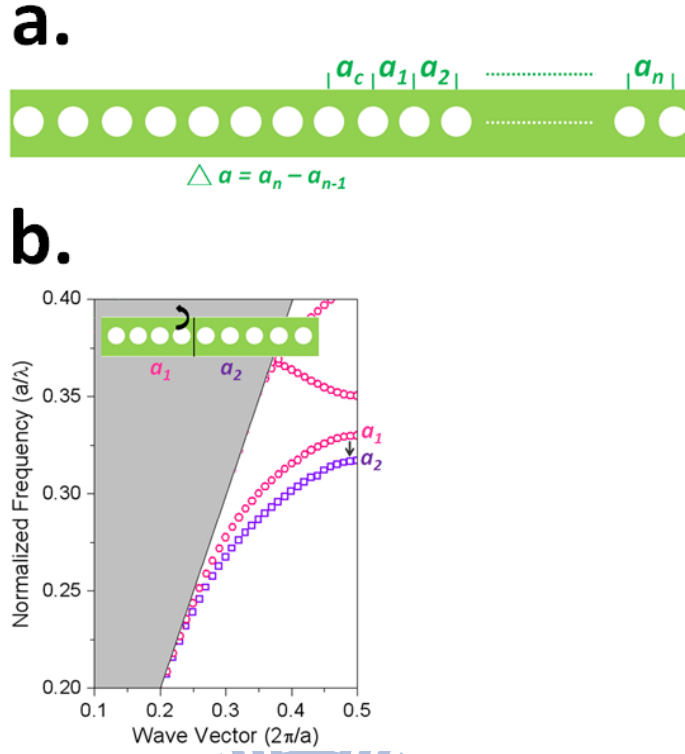
Fig. 3-2: (a) Digital tuning of lattice constant in our nanocavity design. (b) Illustration of mode-gap effect formation via *1D PhCs* with different lattice constants on *NB*.

In our nanocavity design, we apply all-gradual-mirror (all-*GM*), which is different from the generally-used hybrid *GM* / periodic mirror (*PM*). To show their difference, we simulate the *1D PhC NB* nanocavities (dielectric-centered) with all-*GM* and *GM* / *PM* under fixed *1D PhC* period numbers of eight for comparison, as shown in Figs. 3-3(a) and (b). The r/a_c, w, a_c, $\triangle a$, and t are 0.35, 600 nm, 360 nm, 5 nm, and 220 nm. The simulated mode profiles in electric-fields of these two nanocavities are simulated in Figs. 3-3(a) and (b). From the simulated results shown in Table 3-1, nanocavity with all-*GMs* shows better modal performance than that with *GM* / *PM*, including larger Q and smaller V.
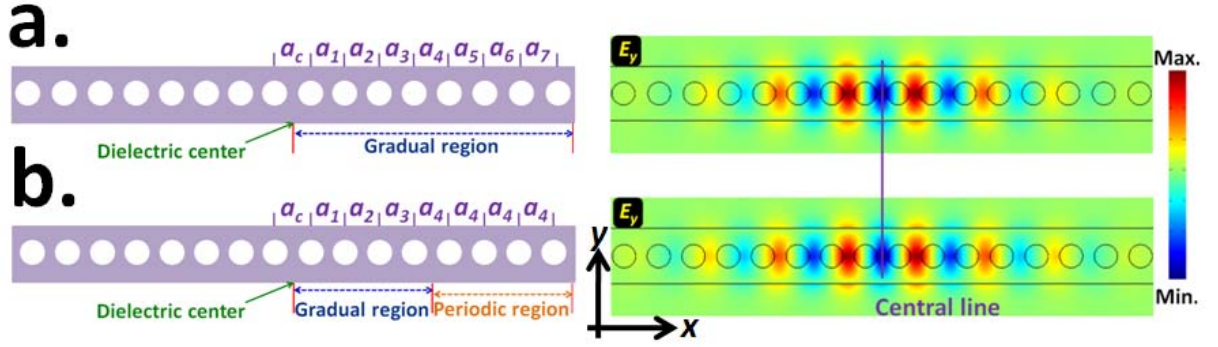
Fig. 3-3: *1D PhC NB* nanocavities with (a) all-*GM* and (b) *GM* / *PM* under fixed *PhC* period numbers of eight.

Table 3-1: Simulation results of the two nanocavities shown in Fig. 3-3.

Types of mirror design	Modal Properties of the 0th – order mode
All-GM	$Q : 5.41 \times 10^3$ $V : 3.64 \times 10^{-1} \, (\lambda / n_{NB})^3$ $\lambda : 1563.5$ nm
GM / PM	$Q : 1.68 \times 10^3$ $V : 4.06 \times 10^{-1} \, (\lambda / n_{NB})^3$ $\lambda : 1560.9$ nm

To further confirm the *PBG* effect formed by the *1D PhC* all-*GM* on *NB* with mode-gap effect, we calculate the transmission spectra of all *GM* with different period numbers, as shown in Fig. 3-4. The input signal is an impulse with Gaussian mode profile, whose central wavelength is 1.5 μm. When the *GM* period increases, a loss suppression of more than two orders of magnitude between 4 and 10 periods can be achieved. Under the reflection provided by the *1D PhC GM* on *NB*, we then discuss several parameters, including *w*, *GM* period number, and *r/a_c*, for optimizing the *1D PhC NB* nanocavities with large *Q/V* value in the following section.
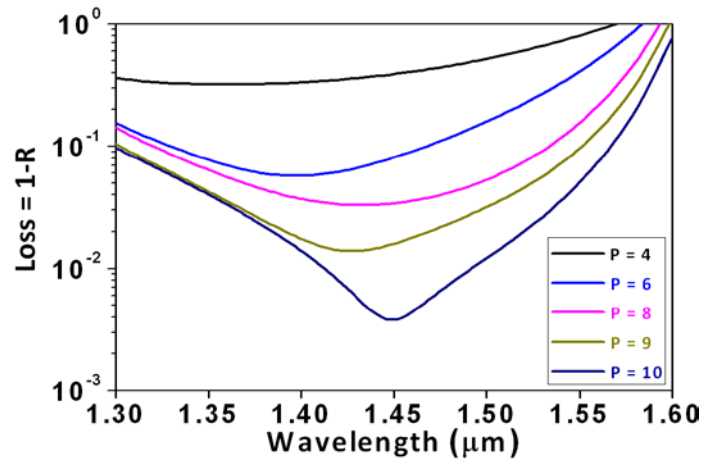
Fig. 3-4: Transmission spectra of *1D PhC GMs* with different periods from 4 to 10. The lattice constant is varied from 360 nm with 5 nm increment under fixed *r*, *w*, and *t* of 126, 600, and 220 nm.
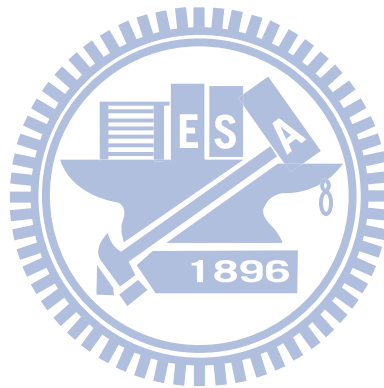
3.3 *1D PhC NB* nanocavities

3.3.1 Simulated Modal Properties

Via *3D FDTD* simulation, the modal properties of the air- and dielectric-centered *1D PhC NB* nanocavities are investigated. Different structural parameters, including *w*, *GM* period number, and r/a_c, are tuned for optimizing the properties of 0th – order mode in nanocavities. At first, *Q* and *V* of the 0th – order mode in these two nanocavities when the beam width *w* is varied from 500 nm to 700 nm are simulated. The parameters a_c, $\triangle a$, *t, GM* period number, and r/a_c, are set as 360 nm, 5 nm, 220 nm, 10, and 0.35. The simulated results are shown in Fig. 3-5. In Fig. 3-5(a), *Q* of the two nanocavities both decrease when *w* increases. This is because that the increased w increases the effective index and leads to enlarged scattering losses in *GM*s. In addition, the difference in *Q* between these two nanocavities can be explained via their time-averaged power flow in z component (S_z) shown in Fig. 3-6. Because the mode distribution S_z in air-centered nanocavity shows nodal lines in symmetric plane according to the far field cancellation [38], the vertical radiation loss can be effectively suppressed. Thus, the air-centered nanocavity shows higher *Q* than that of dielectric-centered nanocavity. And the simulated *V* f the dielectric- and air- centered nanocavities reach their smallest value when w = 550 nm ($V \sim 0.36$ $(\lambda/n_{NB})^3$) and 600 nm ($V \sim 0.39$ $(\lambda/n_{NB})^3$) respectively. Considering for the smallest *V*, we choose *w* = 600 nm in the following optimization work. Within the tuning range of *w*, the highest *Q/V* value for each air- and dielectric-centered *NB* nanocavities are 4.5×10^5 $(\lambda/n_{NB})^{-3}$ and 2.4×10^5 $(\lambda/n_{NB})^{-3}$.

Fig. 3-5: The simulated (a) Q and (b) V of 0th – order mode as the function of w in dielectric- and air-centered *1D PhC NB* nanocavities.
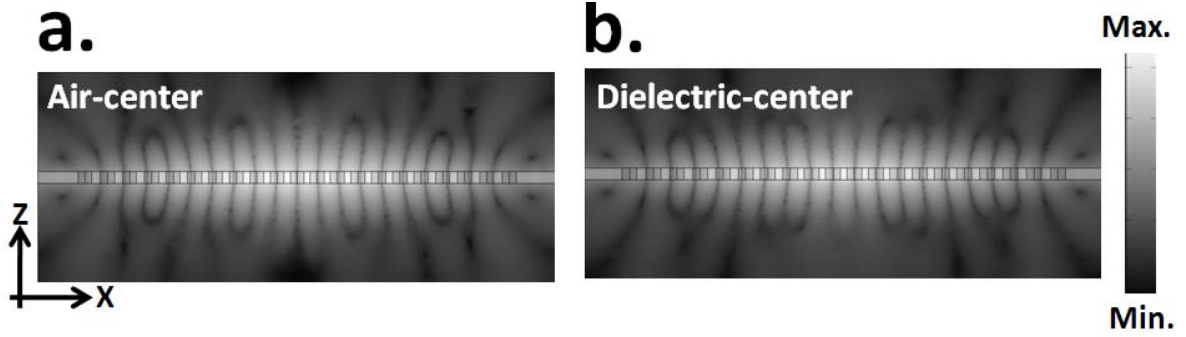
Fig. 3-6: The simulated mode profiles in S_z of air- and dielectric-centered *1D PhC NB* nanocavities in *x-z* plane.

    Then we investigate the modal properties of these nanocavities with different *GM* periods, as shown in Fig. 3-7. The parameters a_c, $\triangle a$, *t*, *w*, and r/a_c, are set as 360 nm, 5 nm, 220 nm, 600 nm, and 0.35. In Fig. 3-7, Q increases with the *GM* periods and saturates when *GM* periods > 13. Moreover, λ and V also increase with the *GM* periods increases and saturates when *GM* periods > 7. The saturations in λ and V also imply that the 0th – order mode in *1D PhC NB* nanocavities is a localized mode, as shown in Fig. 3-7(d). Thus the further addition of *GM* periods larger than seven cannot be experienced by the 0th – order mode. During the optimization of the *GPs*, the highest Q/V value for air- and dielectric-centered *1D PhC NB* nanocavities are 1×10^6 $(\lambda/n_{NB})^{-3}$ and 4×10^6 $(\lambda/n_{NB})^{-3}$ respectively.
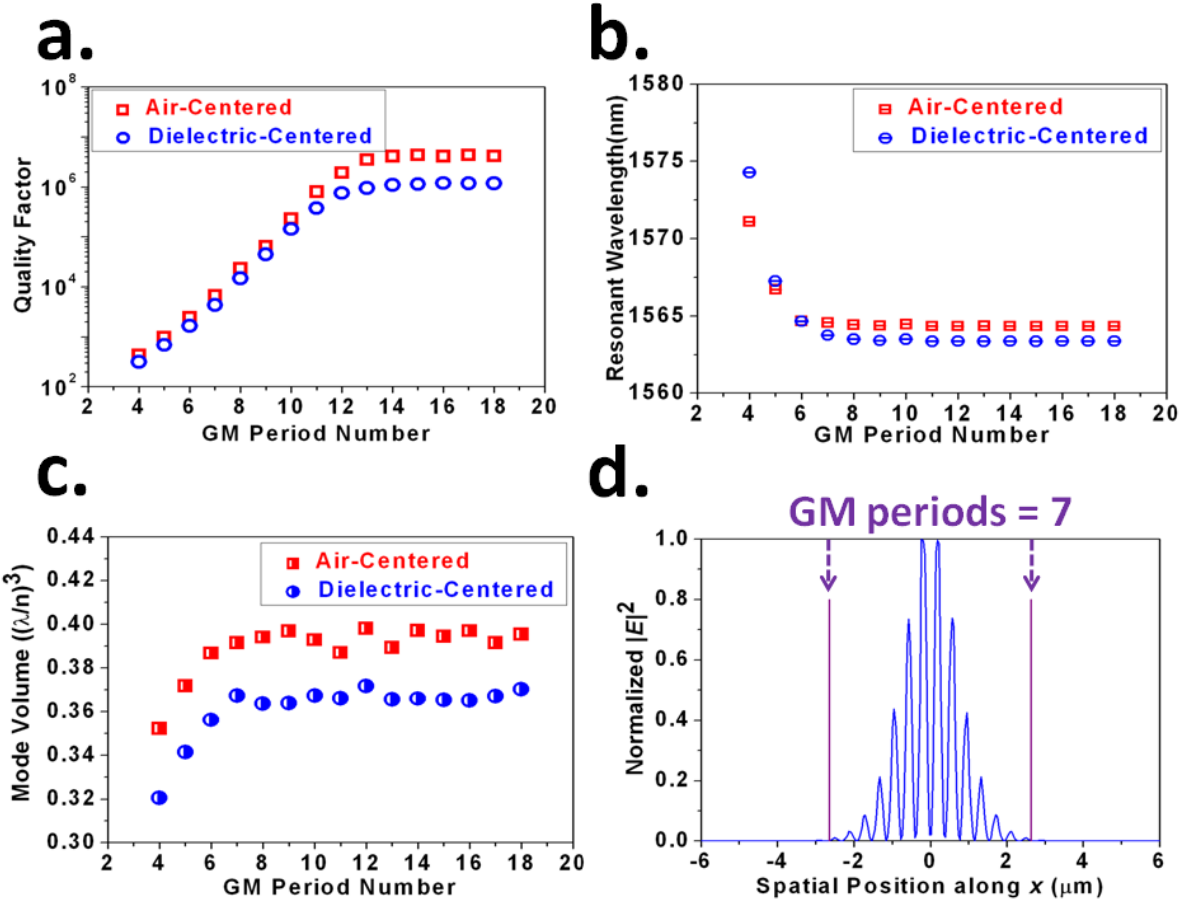
Fig. 3-7: The simulated (a) Q, (b) V, and (c) λ of 0th – order mode as the function of *GM* periods in air- and dielectric-centered *1D PhC NB* nanocavities. (d) The simulated $|\vec{E}|^2$ of 0th – order mode in electric field in air-centered *1D PhC NB* nanocavity with 14 *GM* periods.

Furthermore, we also investigate the influence of r/a_c on the modal properties of air- and dielectric- centered *1D PhC NB* nanocavities, as shown in Figs. 3-8(a) and (b). The parameters a_c, $\triangle a$, t, w, and *GM* period number are set as 360 nm, 5 nm, 220 nm, 600 nm, and 14. In Figs. 3-8(a) and (b), the Qs of these two nanocavity designs reach their optimized values of 4.98×10^6 and 1.38×10^6 both when $r/a_c = 0.29$. Two mechanisms are responsible for the Q variation. One is that the modulation strength of effective index becomes smaller as r/a_c increase and Q would increase due to the reduced mode mismatch. Another one is that the total effective index of *NB* structure would decrease as r/a_c increase and Q would decrease due to the reduction of total-internal-reflection confinement. The simulated V of these two nanocavity designs both decrease when r/a_c increases, which is owing to the volume

shrinkage of the dielectric material in cavity region. During the optimization of r/a_c, the highest Q/V value for air- and dielectric-centered *1D PhC NB* nanocavities are 2.9×10^6 $(\lambda/n_{NB})^{-3}$ and 9.9×10^6 $(\lambda/n_{NB})^{-3}$.
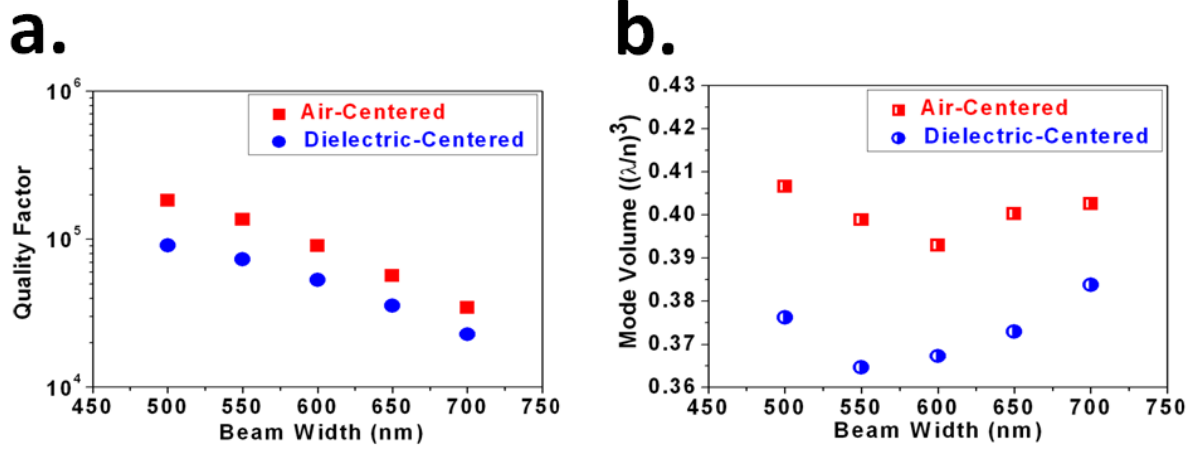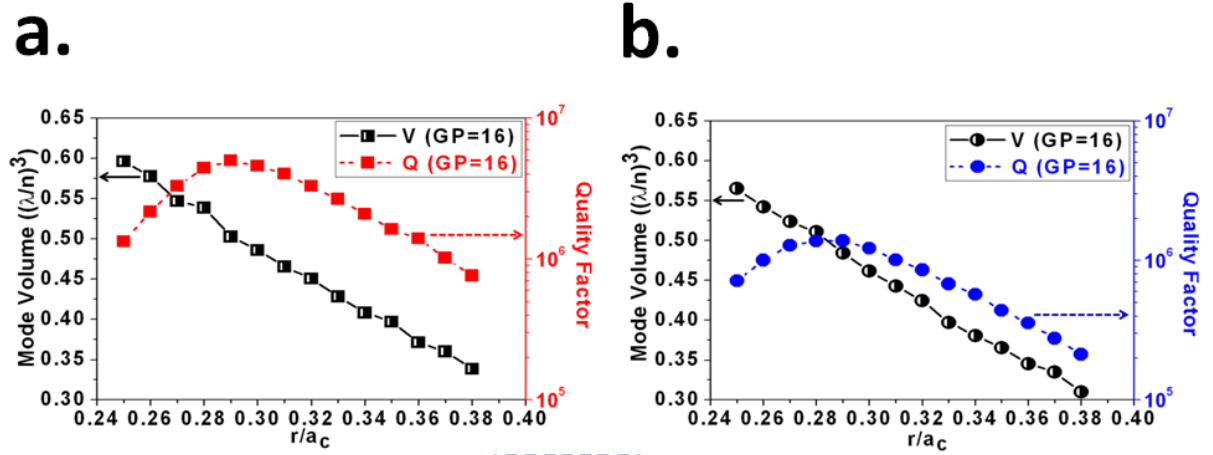

Fig. 3-8: The Q and V of 0th – order mode as the function of r/a_c in (a) air- and (b) dielectric-centered *1D PhC NB* nanocavities.
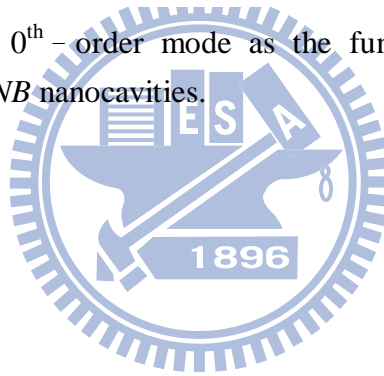
3.3.2　Measurement Results and Discussions for Laser Application

Referring to the simulation results, the air- and dielectric-centered *1D PhC NB* nanocavities are realized on a *InGaAsP MQWs* suspended *NB*. To characterize the devices, a near-infrared micro-photoluminescence system is utilized. Experimental results will be confirmed via *FDTD* and *FEM* simulations.

To keep the device size compact, we choose *1D PhC NB* nanocavities with 8 *GM* periods in our experiment. The length of the *NB* is only 6 μm, which is very beneficial for serving as a nanolaser in condensed photonic integrated circuits (*PIC*s). The scanning electron microscope (*SEM*) pictures of air- and dielectric-centered *1D PhC NB* nanocavities are shown in Figs. 3-9(a) and (b). Their r/a_c and w are 0.37 and 690 nm.

In measurements, the lasing spectrum of air-centered *1D PhC NB* nanocavity in Fig. 3-10(a) shows single mode lasing with side mode suppression ratio (*SMSR*) of 14 dB at 1555.5 nm. The light-in and light-out (*L-L*) curve in Fig. 3-10(b) shows a low threshold of 350 μW. Moreover, the lasing spectra under different pump power from 1.67 mW to 3.8 mW are shown in Fig. 3-11. Only one lasing peak is observed, which confirms the single mode lasing.
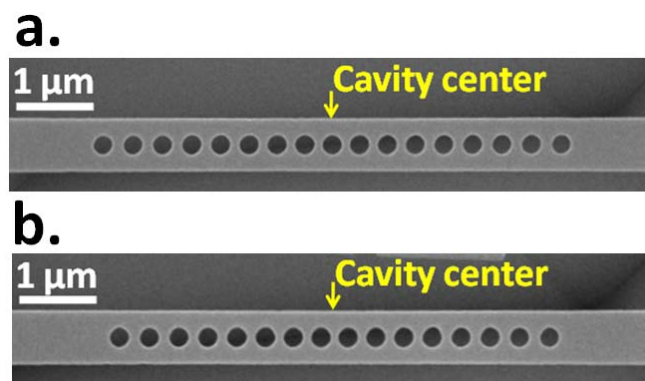
Fig. 3-9: *SEM* pictures of (a) air- and (b) dielectric-centered *1D PhC NB* nanocavities with 8 *GM* periods.
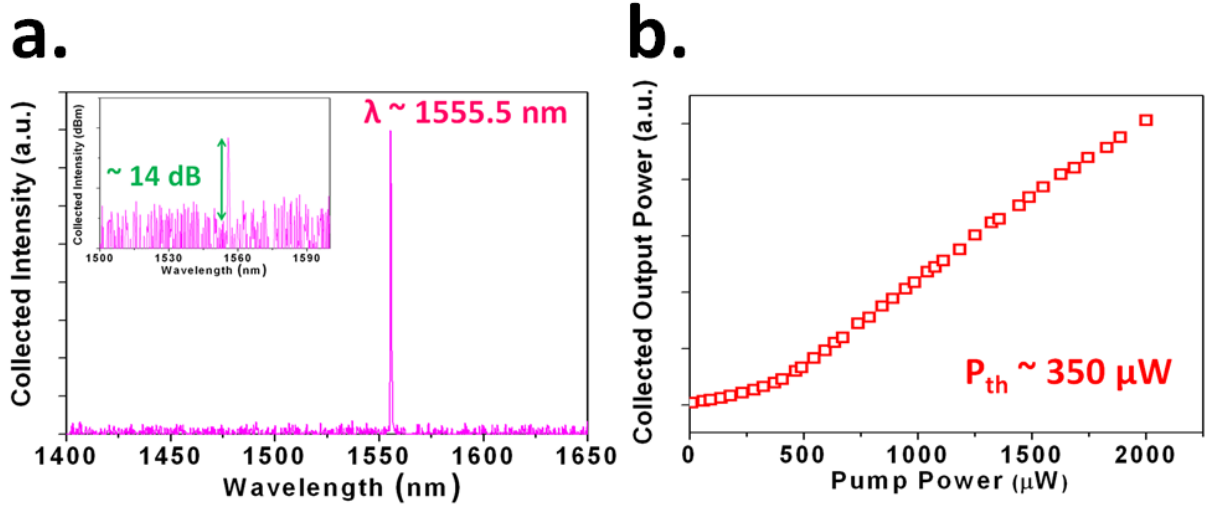
Fig. 3-10: Lasing characterization of air-centered *1D PhC NB* nanocavity with $r/a_c = 0.37$ and $w = 690$nm. (a) Under the pump power of 1.5 mW, the lasing spectrum is shown and its inset shows the *SMSR*. (b) The *L-L* curve shows the lasing threshold of 350 μW.
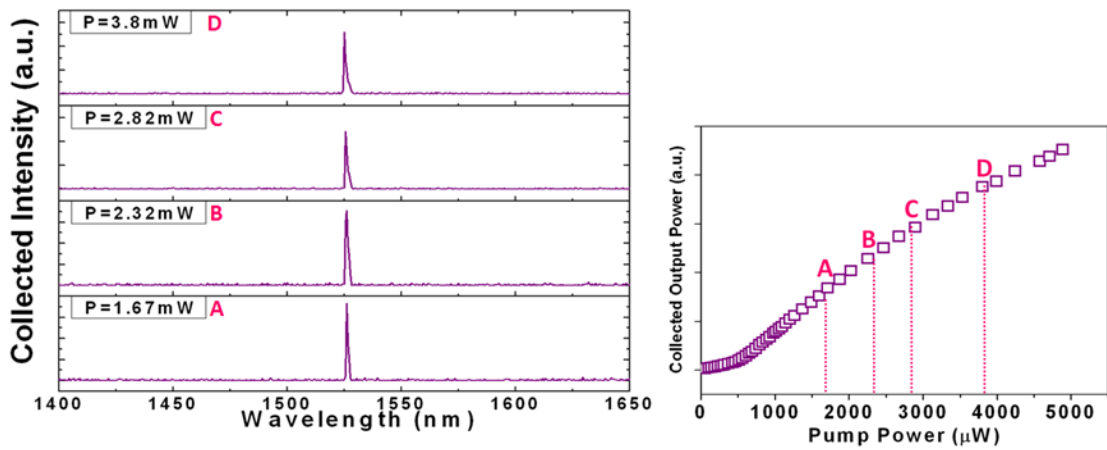
Fig. 3-11: Lasing spectra under different pump powers, which confirms the single mode lasing.

In addition, we also show the lasing properties of dielectric-centered nanocavity design for comparison. In Fig. 3-12(a), single mode lasing with higher *SMSR* of 24 dB at 1546.5 nm is observed. In Fig. 3-12(b), the *L-L* curve shows a lasing threshold of 461 μW. Comparing these values with those of air-centered nanocavity in Fig. 3-10, we can see that the air-centered nanocavity has smaller *SMSR* but lower threshold than that of dielectric-centered nanocavity. This is mainly attributed to the higher *Q* of air-centered nanocavity than that of dielectric-centered nanocavity. To confirm this, we compare the thresholds between air- and

dielectric-centered nanocavities under the same parameters, as shown in Fig. 3-13. In each comparison, the lasing threshold of air-centered nanocavity is always smaller than that of dielectric-centered nanocavity, which confirms this phenomenon. Among these laser devices, the lowest threshold of 292 μW is observed from an air-centered nanocavity.
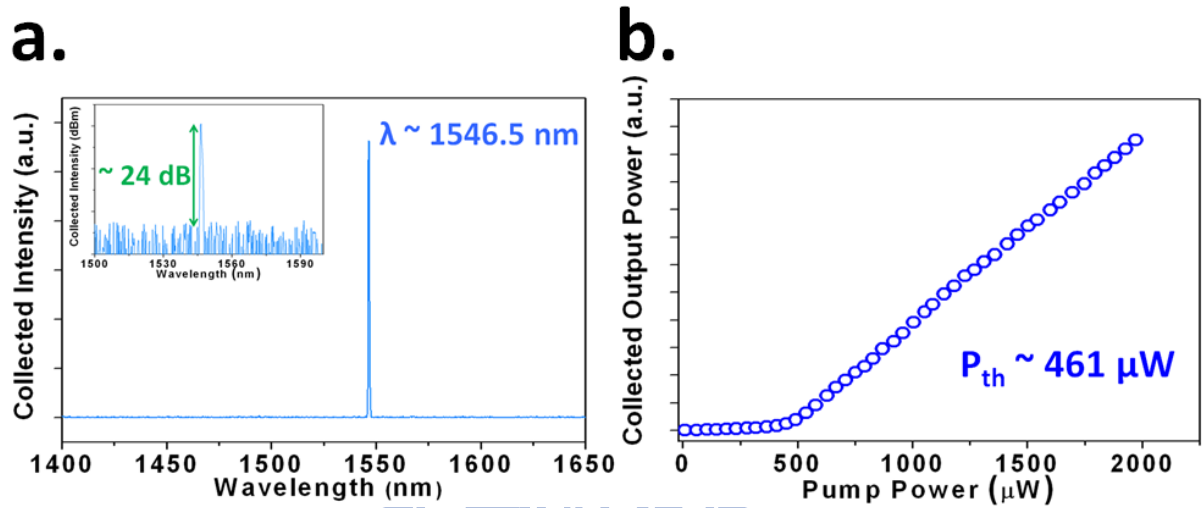
Fig. 3-12: Lasing characterization of dielectric-centered *1D PhC NB* nanocavity with r/a_c = 0.37 and w = 690nm. (a) Under the pump power of 1.5 mW, the lasing spectrum is shown and its inset shows the *SMSR*. (b) The *L-L* curve shows the lasing threshold and its inset shows polarization of laser emission.
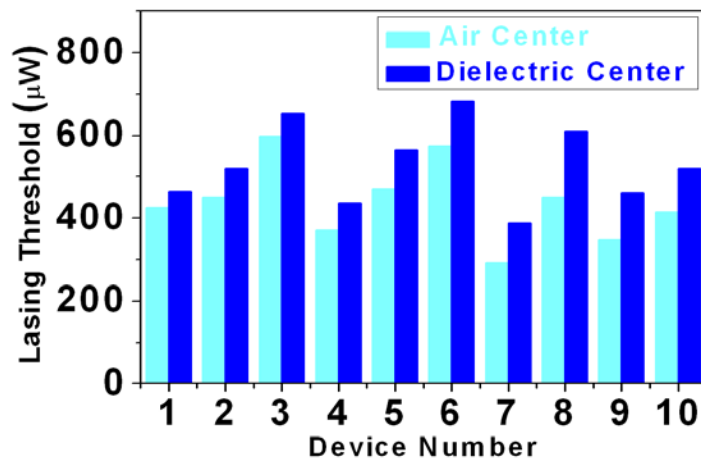
Fig. 3-13: Lasing threshold comparison between the air-center and dielectric-center nanocavity designs.
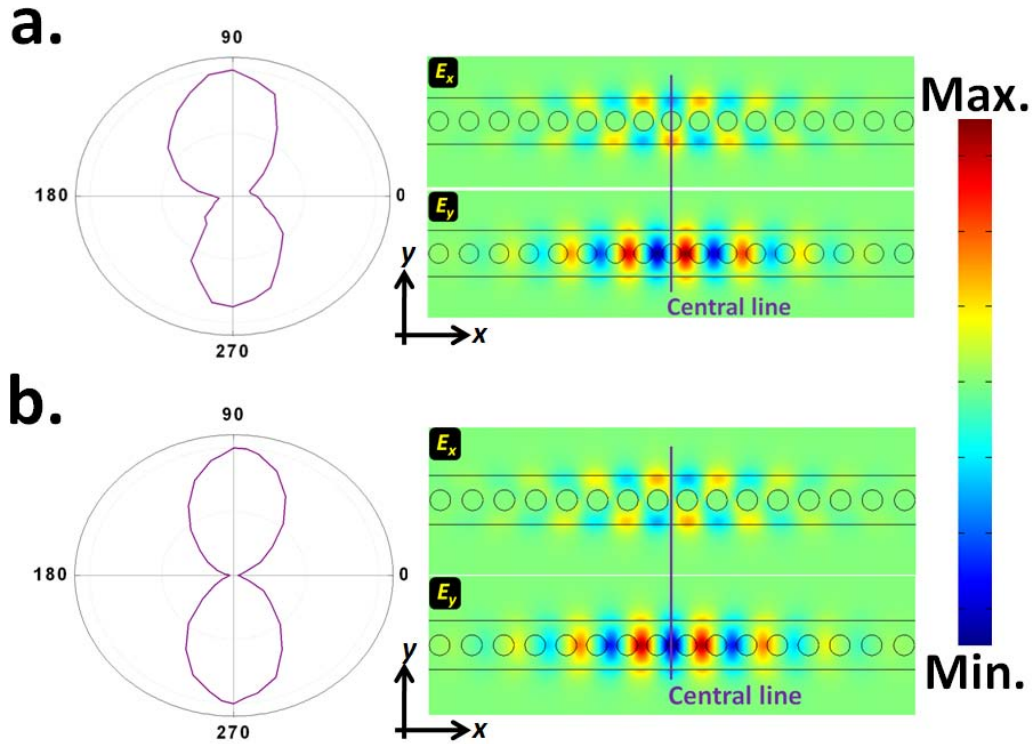
Fig. 3-14: The measured polarizations of (a) air- and (b) dielectric-centered *1D PhC NB* nanocavities. The simulated mode profiles in E_x and E_y are shown as the insets of (a) and (b)

Moreover, the measured polarization of air- and dielectric-centered *1D PhC NB* nanocavity are both *y*-polarized with polarization degree of 1 : 11 and 1 : 36, as shown in Figs. 3-14(a) and (b). The *y*-polarization is the nature of waveguide-based nanocavity, which is owing to the dominant E_y than E_x of the mode, as shown in the insets of Figs. 3-14(a) and (b).

In addition, the measured lasing wavelength of these two nanocavities under different r/a_c and *w* also show good matching with the simulation results, as shown in Figs. 3-15 (a)-(d). The increasing *w* and decreasing *r/a* will increase the effective refractive index of the nanocavity. Therefore, we observe that lasing wavelength increases when *w* increases and r/a_c decreases. The difference between the simulated and measured results may result from the fabrication imperfections, including surface roughness, slight hole-size variation, and so on.
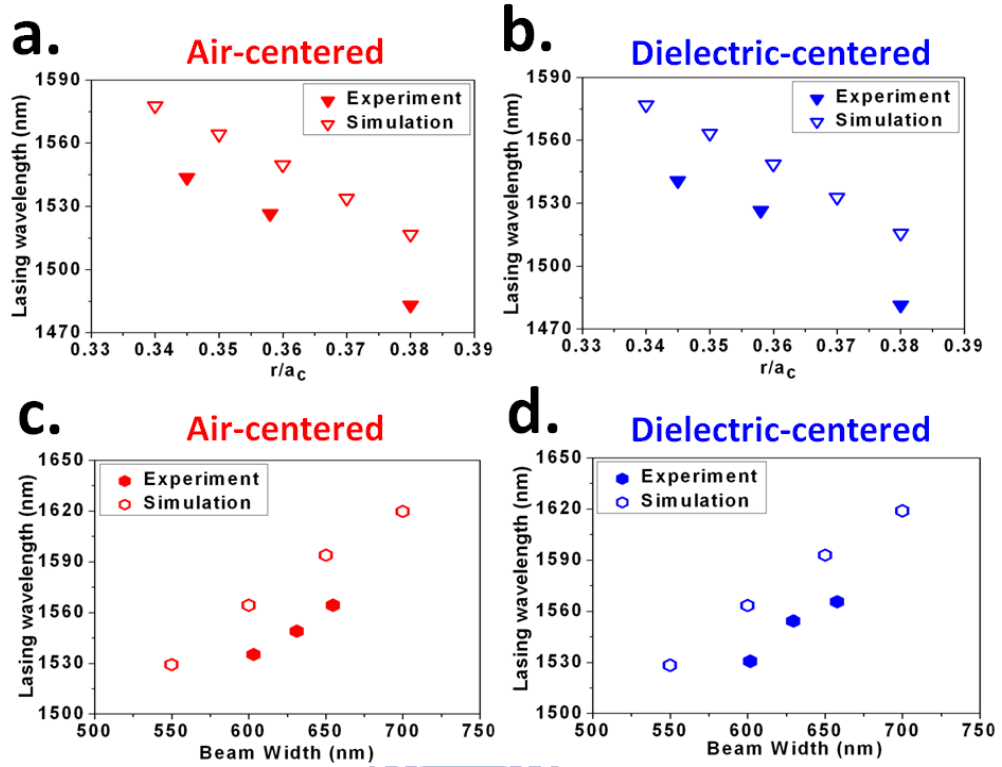
Fig. 3-15: The lasing wavelength of 0th – order mode as the function of (a), (b) *r/a* and (c), (d) *w* in air- and dielectric-centered *1D PhC NB* nanocavities.

We also investigate on the effect of adding the outer *PM* with two and six periods in dielectric-centered *1D PhC NB* nanocavities with all-*GMs*. The parameters a_c, $\triangle a$, *t, w, GM* period number and r/a_c, are 360 nm, 5 nm, 225 nm, 670 nm, 8, and 0.39. Some interesting observations are illustrated in the following. First, extra *PM* increases the total *NB* length,
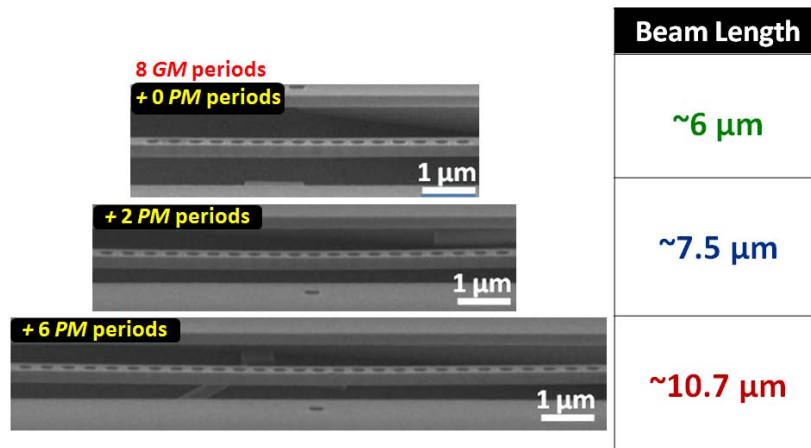
Fig. 3-16: The *SEM* pictures of dielectric-centered *1D PhC NB* nanocavities with different extra *PM* periods of zero, two, and six.
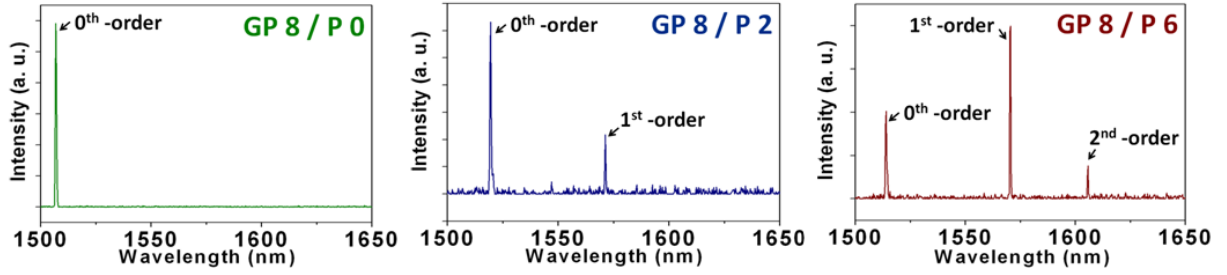
Fig. 3-17: The lasing spectra of dielectric-centered *1D PhC NB* nanocavities with different *PM* periods under the pump power of 1.5 mW. The 1st – and 2nd – order mode lasing can be observed in sequence when the *PM* period increase from zero to six.

which leads to a fragile structure, as shown in Fig. 3-16. This also lets this structure not suitable for the optofluidic application due to the external force from the environment. Second, high order modes will appear and lead to multimode lasing. As shown in Fig. 3-17, for the nanocavity with outer *PMs* (two and six periods), the high-order modes, including 1st – and 2nd – order modes are observed in the lasing spectra, results from the *Q* enhancements for the high-order modes due to extra *PMs*.

The simulated *Q* of different order modes in dielectric-centered *1D PhC NB* nanocavities with zero, two, and six *PM* periods are listed in table 3-2. The *Qs* of different order modes become larger than 10^3 when the *PM* period increases from zero to six. Thus, the 0th – , 1st – and 2nd – order modes in lasing spectra are observed in sequence when the *PM* period increases. Third, moving the pump spot along the *NB* (*x*-direction) will lead to 0th – order

Table 3-2: The simulated *Q* of different order modes in dielectric-centered *1D PhC NB* nanocavities with different *PM* periods.

Different order modes / *PM* periods	0th – order mode	1st – order mode	2nd – order mode
0	5.18×10^3	5×10^2	1.48×10^2
2	4.50×10^4	2.26×10^3	4.11×10^2
6	1.25×10^5	4.10×10^4	1.86×10^3

mode suppression. The size of pump spot is approximately 4.2 μm and the dielectric-centered *1D PhC NB* nanocavity with ten *PM* periods is used, as shown in Fig. 3-18(a). The parameters of nanocavity including a_c, $\triangle a$, t, w, *GM* period number, and r/a_c, are 360 nm, 5 nm, 225 nm, 660 nm, 8, and 0.36. When the pump spot is moved from 0 nm (center of the cavity) to 1350 nm, the 0th – order mode is suppressed while the 1st – order mode is still observed. The varied spectra are shown in Figs. 3-18(b)-(g). The mode suppression is caused by the different mode distribution of the 0th – and 1st – order modes shown in Figs. 3-19(a) and (b). When the pump spot is moved away from the cavity center, the pumping for the 0th – order mode becomes insufficient, while that for the 1st – order modes becomes sufficient. This observation also confirms again that the 0th – order mode localizes in the cavity region.
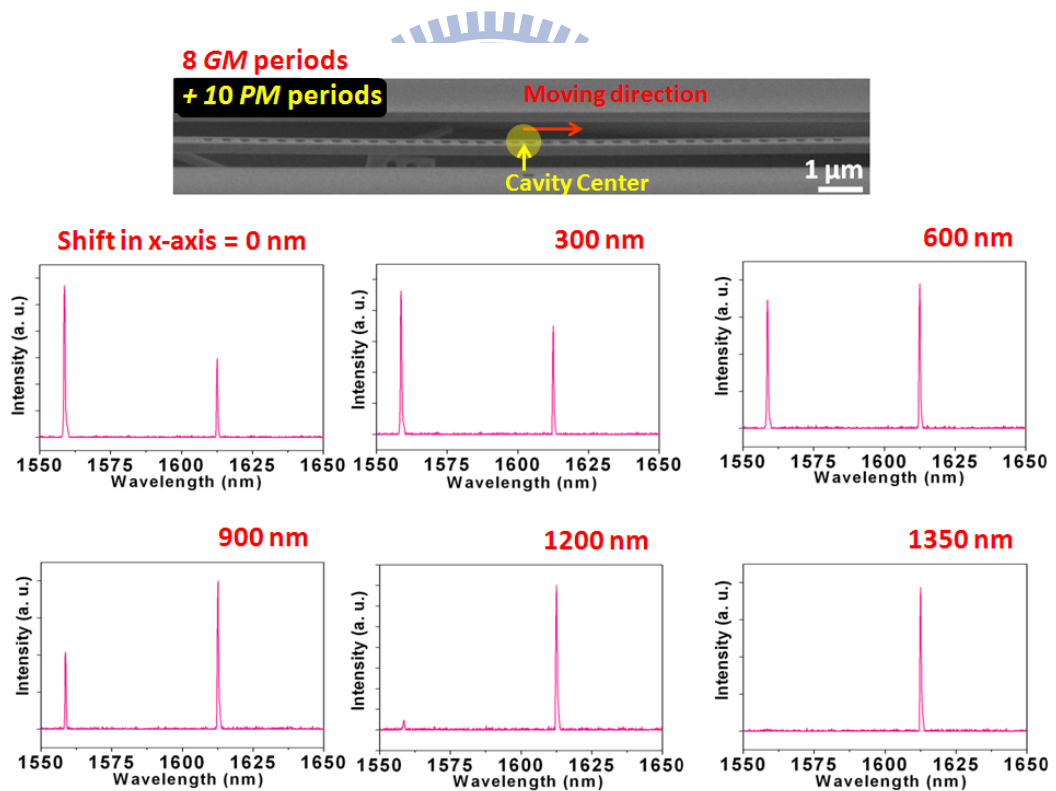
Fig. 3-18: (a) *SEM* picture of dielectric-centered *1D PhC NB* nanocavity and the scheme of pump spot moving along the *NB*. (b)-(g) The lasing spectra when with the pump spot moves from 0 nm to 1350 nm away from the cavity center along *x*-axis.
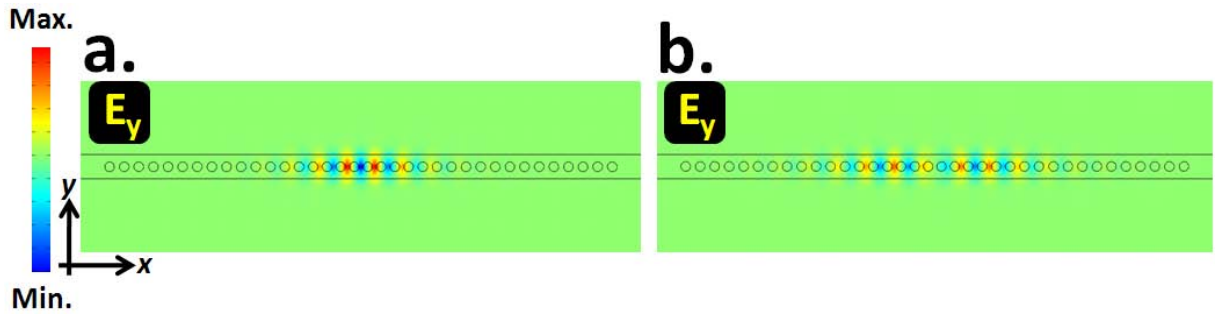
Fig. 3-19: The simulated mode profile in E_y field of (a) the 0th – order and (b) the 1st – order modes in dielectric-centered *1D PhC NB* nanocavity.

3.4 Summary

In this chapter, we have proposed air-centered and the dielectric-centered *1D PhC NB* nanocavities. In simulations, the maximum *Q/V* value for air-centered and the dielectric-centered nanocavities are 2.9×10^6 $(\lambda/n_{NB})^{-3}$ and 9.9×10^6 $(\lambda/n_{NB})^{-3}$. To achieve ultra-small device footprint, we realize *1D PhC NB* nanocavities with 8 *GM* periods. In measurements, we observe the single mode lasing actions with low thresholds from air- and dielectric-centered nanocavities. From the air-centered nanocavity, the lowest lasing threshold of 292 μW is observed. Therefore, we believe it will be a good candidate for the efficient nanolaser in condensed *PICs*.
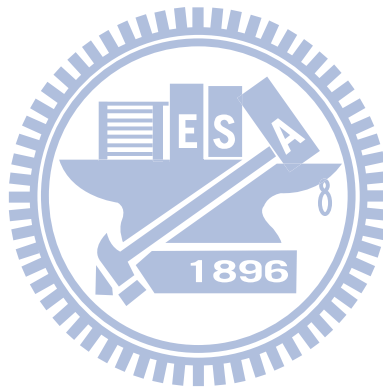
Chapter 4 Index Sensing via Coupled-*NB* Nanocavities

4.1 Introduction

In this chapter, we propose *1D PhC* coupled-*NB* nanocavity for optical sensing application. From simulations, we address the coupled 0th – order lasing modes in measurements and show the influence of pump spot site on the lasing modes. Then we utilize the glucose water solutions with different concentrations for the optical index sensing. The measured sensitivities are compared with the simulation results.

4.2 Modal Properties of *1D PhC* Coupled-*NB* Nanocavity

We apply the air-centered nanocavity design in chapter 3 to realize the *1D PhC* coupled-*NB* nanocavity. The parameter definition of *NB* thickness (*t*), width (*w*), central lattice constant (a_c), spacing of lattice constant ($\triangle a$), gradual-mirror (*GM*) period number, and air-hole radius over lattice constant (*r/a*) are the same with those in chapter 3. The new parameter beam gap *g* is the spacing of two beams in *1D PhC* coupled-*NB* nanocavity. The parameters *t*, *w*, a_c, $\triangle a$, *GM* period number, and *r/a* are set as 220 nm, 655 nm, 360 nm, 5 nm, 10, and 0.347 in the following simulation. The simulated mode profiles in E_y fields of the even and odd modes in coupled-*NB* nanocavity are shown in Figs. 4-1(a) and (b). From the even mode, the significant electric field distribution in the beam gap would be beneficial for serving as an optical sensor. In Figs. 4-2(a) and (b), we also plot $|E|^2$ distribution of the even and odd modes in coupled-*NB* nanocavity with *g* = 150 nm along the cross line shown in Figs. 4-1(a) and (b) to indicate the electric field enhancement of the even mode in the beam gap region. When the beam gap becomes smaller, the electric field enhancement of even mode in the beam gap region will increase, as shown in Figs. 4-3(a) and (b).
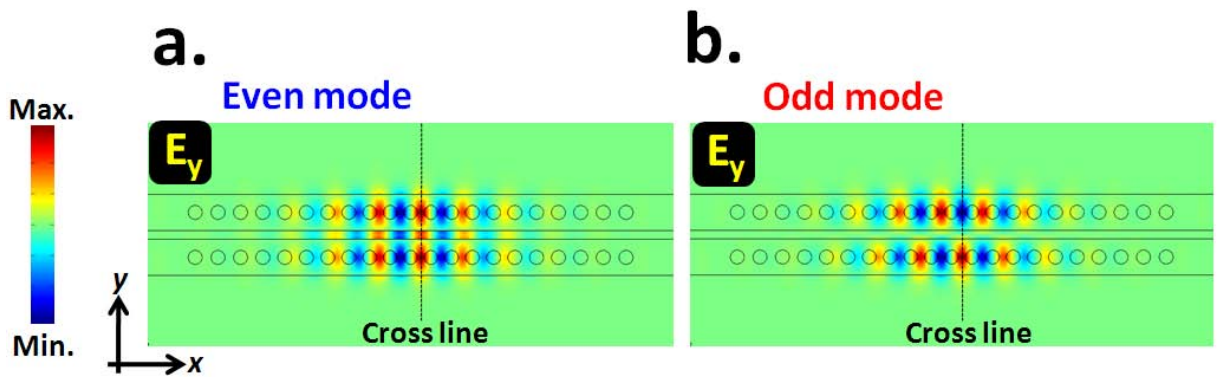
Fig. 4-1: The simulated E_y fields of (a) even and (b) odd modes in *x-y* plane.
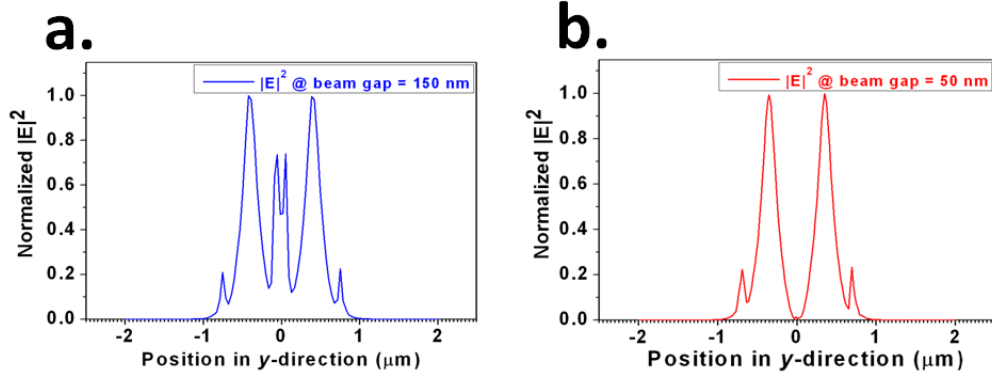
Fig. 4-2: The simulated $|E|^2$ distribution of the (a) even and (b) odd modes in coupled-*NB* nanocavity with $g = 150$ nm along the cross line in Fig. 4-1.
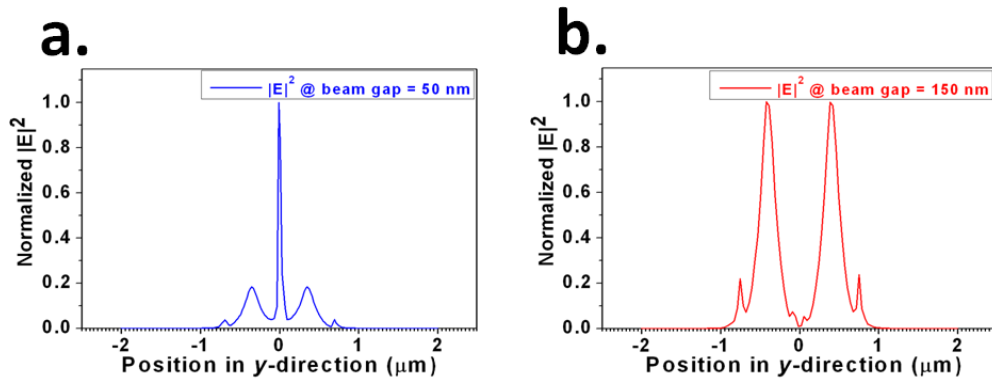
Fig. 4-3: The simulated $|E|^2$ distribution of the (a) even and (b) odd modes in coupled-*NB* nanocavity with $g = 50$ nm along the cross line in Fig. 4-1.

In real cases, the beam widths in *1D PhC* coupled-*NB* nanocavity would not be exactly the same due to the fabrication imperfection, as shown in Fig. 4-4(a). To know the modal properties in asymmetric coupled-*NB* nanocavity, *w* of the two beams are set to be 655 and 670 nm in the following simulations. In the following simulations, the parameters are the same with those mentioned previously. We find two coupled 0th – order modes named as even-like and odd-like modes as shown in Figs. 4-4(b) and (c). The electric fields of these two modes tend to concentrate in one of the beams, which is different from those in symmetric coupled-*NB* nanocavity. However, the electric field of the even-like mode still concentrates more in the beam gap than odd-like mode. In addition, the electric field distribution of the even-like mode in the beam gap region increases when the beam gap decreases, as shown in Figs. 4-6(a).
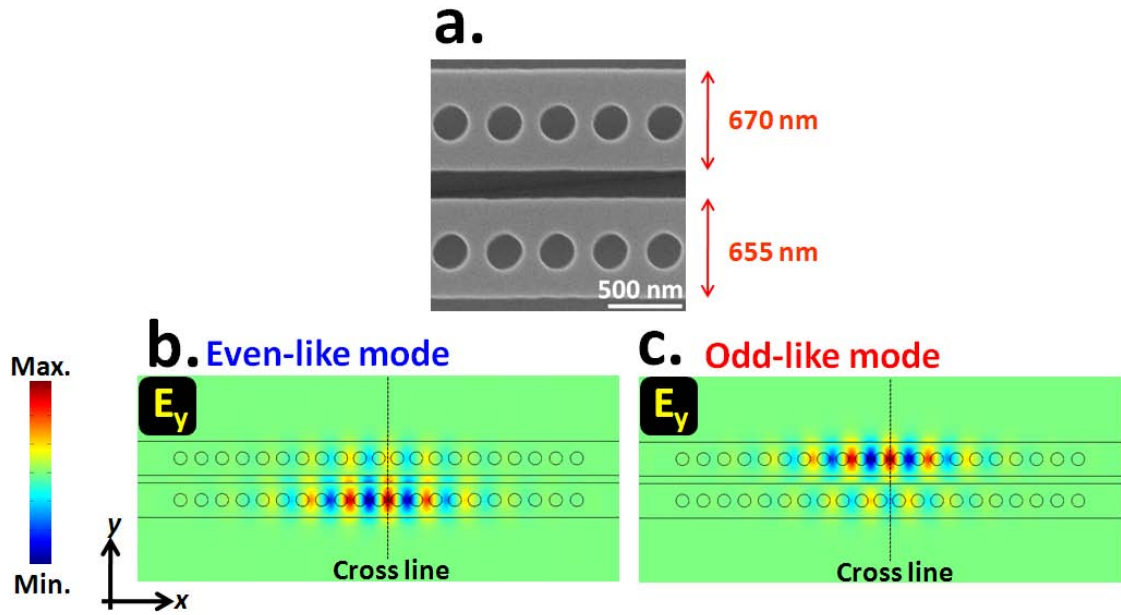
Fig. 4-4: (a) *SEM* picture of *1D PhC* coupled-*NB* nanocavities with *r/a* = 0.347 and *g* = 210 nm. The simulated mode profile in E_y field of the (b) even-like and (c) odd-like modes in asymmetric coupled-*NB* nanocavity shown in (a).
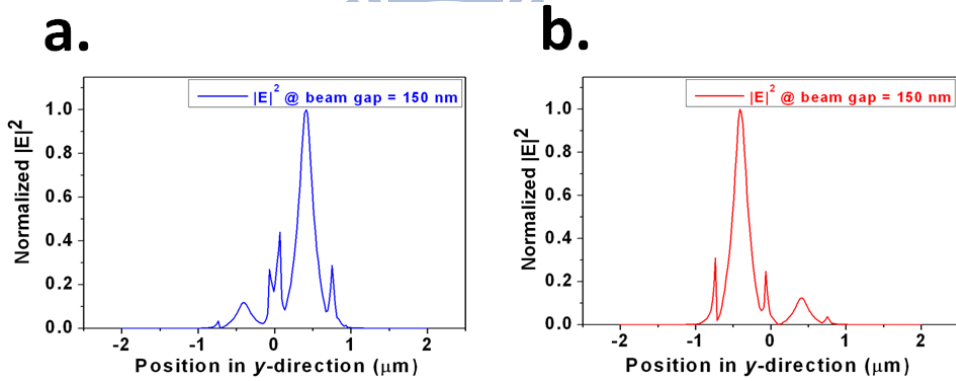
Fig. 4-5: The simulated $|E|^2$ distribution of the (a) even-like and (b) odd-like modes in asymmetric coupled-*NB* nanocavity with *g* =150 nm along the cross line in Fig. 4-4.
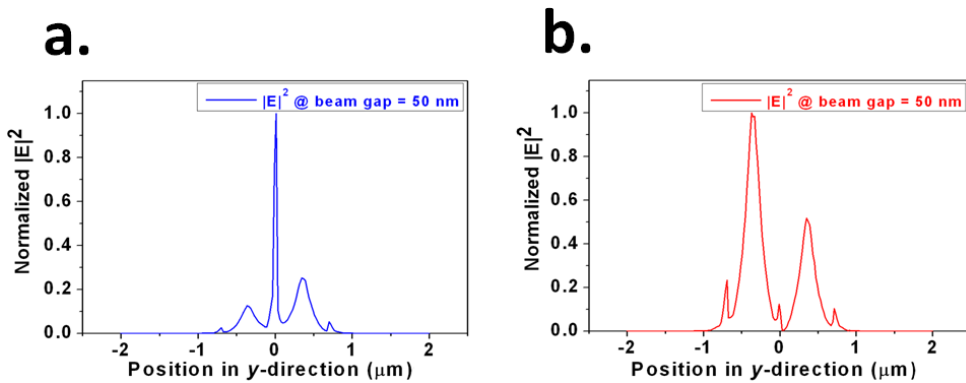
Fig. 4-6: The simulated $|E|^2$ distribution of the (a) even-like and (b) odd-like modes in asymmetric coupled-*NB* nanocavity with *g* = 50 nm along the cross line in Fig. 4-4.
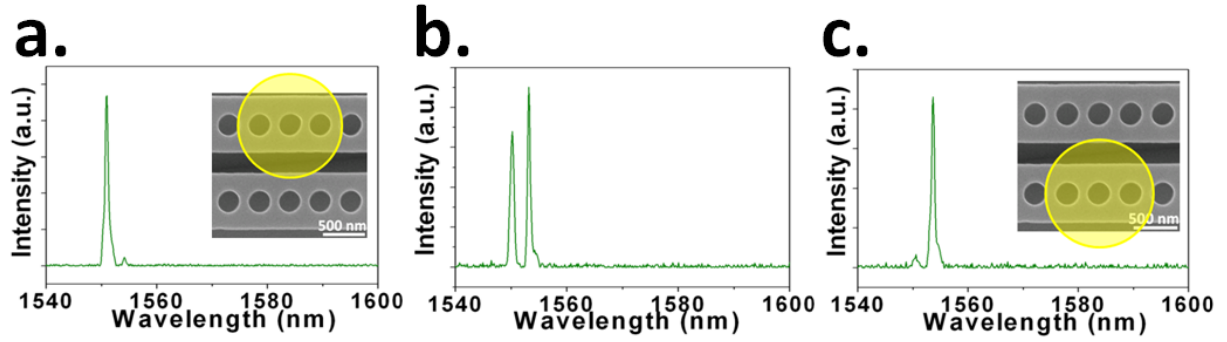
Fig. 4-7: The lasing spectra under different pump spot position along *y*-direction. The pump power is fixed at 2 mW.

In measurement, we find that these asymmetric mode distributions will lead to pump position sensitive lasing spectra. In experiments, the pump spot is moved along the y-direction via piezo-stage. Scheme and corresponding lasing spectra are show in Figs. 4-7(a)-(c). *SEM* picture of the characterized device with asymmetric *NB* (*w* = 651 nm and 656 nm) is also shown in Fig 4.8(a). In Fig. 4-7, we can observe the coupled modes (even- or odd-like) will become the dominant lasing mode when the pump spot is moved to the beam their electric-fields concentrated on, as shown by the schemes in Figs. 4-7(a) and (c). These experimental observations agree with the simulation results and indicate that we can control the lasing behaviors by different non-uniform pump conditions.
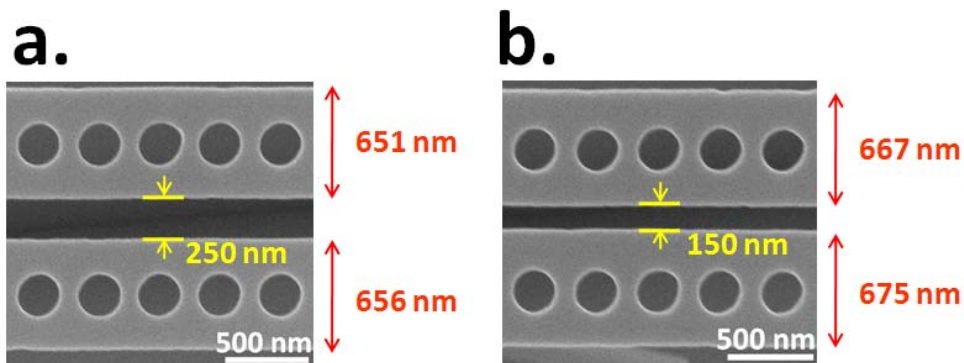
Fig. 4-8: *SEM* pictures of *1D PhC* coupled-*NB* nanocavities with (a) *r/a* = 0.364, *g* = 250 nm and (b) *r/a* = 0.347, *g* = 150 nm.

In addition, we also measure the coupled-*NB* nanocavity with small beam gap of 150 nm. *SEM* picture of the characterized device is also shown in Fig 4.8(b). The beam widths *w* are 667 and 675 nm respectively. In measurements, the lasing wavelengths of odd-like and even-like modes are 1571.6 and 1578.2 nm with wavelength difference of 6.6 nm, as shown in Fig. 4-9(a). To verify the measured results, we simulated the wavelength difference of these two modes in the nanocavity shown in Fig. 4-8(b) as function of the beam gap, as shown in Fig. 4-9(b). When g =150 nm, the measured wavelength difference of 6.6 nm matches well with the simulated result of 7.4 nm. We also list the comparisons of measured and simulated wavelength difference under beam gap in Table 4-1, which shows good matches and unique feature of the coupled mode.
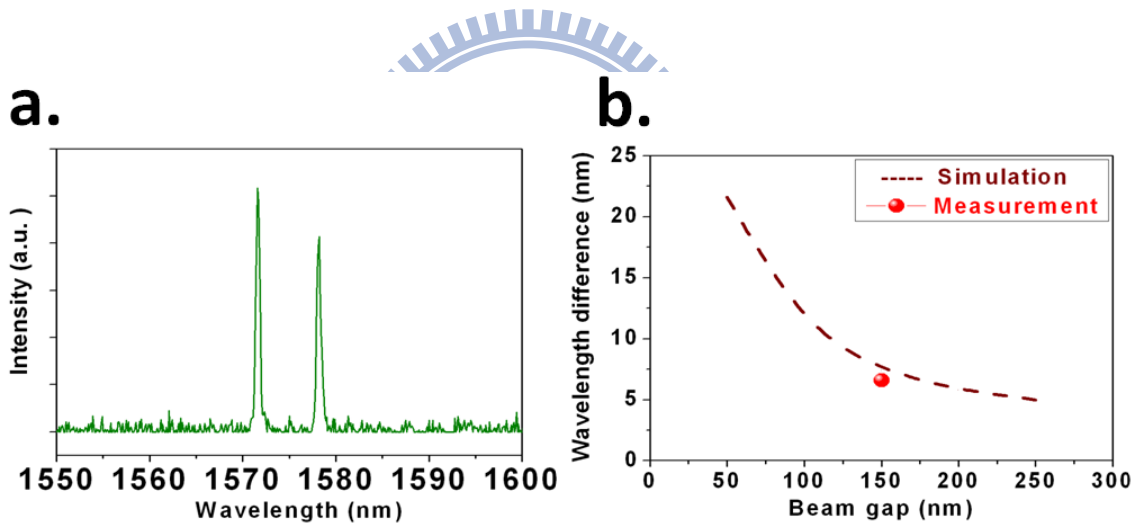
Fig. 4-9: (a) Laing spectrum from the even-like and odd-like modes in asymmetric *1D PhC* coupled-*NB* nanocavity under the pump power of 1.78 mW. (b) The simulated wavelength difference between the even-like and odd-like modes of the nanocavity shown in Fig. 4-8(b) as function of the beam gap. The measured wavelength difference when $g = 150$ nm matches well with the simulation result.

Table 4-1: Simulated and measured wavelength difference of the asymmetric *1D PhC* coupled-*NB* nanocavities with different parameters.

Beam widths (nm)	Beam gap (nm)	r/a_c	Simulated wavelength difference (nm)	Measured wavelength difference (nm)
667 / 675	150	0.364	7.4	6.6
655 / 670	210	0.347	8.8	9.6
655 / 665	220	0.347	6.42	5.85

4.3 Optical Sensing Measurement

For *PhC* cavity, it can serve as a good candidate for sensor due to its wavelength-scale device size, ultra-high *Q*, and localized mode field, which are beneficial for high sensitivity to the environmental index variation. The sensitivity R_n is defined as the resonant wavelength (λ_r) shift (nm) per refractive index unit (*RIU*). And the minimum detectable refractive index variation Δn_{det} represents how small the refractive index variation that the optical sensor can detect.

These two factor can be expressed as :

$$R_n = \frac{\Delta \lambda_n}{\Delta n} \tag{4-1}$$

$$\Delta n_{det} = \frac{\Delta \lambda_{FWHM}}{R_n} = \frac{\lambda_r}{Q R_n} \tag{4-2}$$

where $\Delta \lambda_n$ is the wavelength shift caused by the refractive index variation Δn and $\Delta \lambda_{FWHM}$ is the spectral linewidth of the resonant mode.

In 2009, the slotted *PhC* cavity has been demonstrated in optical sensing and the sensitivity is as high as 1538 nm/*RIU* in experiments [11]. This high sensitivity results from the large distribution in the slot. Thus, we utilize the *1D PhC* coupled-*NB* nanocavity with the slot-like beam gap in optical sensing via glucose water solutions with different concentrations.

The sensing measurements is performed via the air-centered *1D PhC* coupled-*NB* nanocavity under different environmental refractive indices of *n* = 1 (air), 1.31097 (water), 1.3165 (5 *wt*% glucose water solution), and 1.33441 (20 wt% glucose water solution) [39].
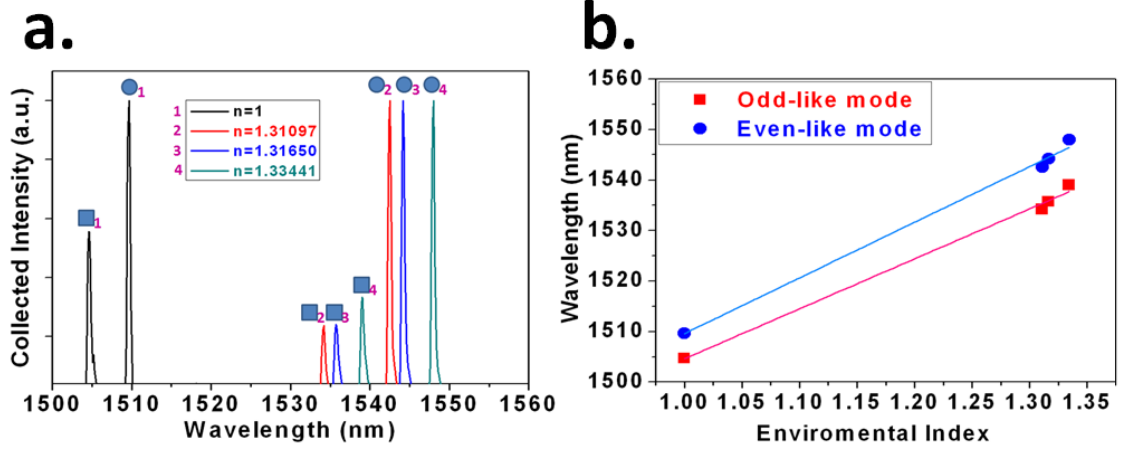
Fig. 4-10:   (a)The lasing spectra of air-centered *1D PhC* coupled-*NB* nanocavity under different environmental refractive indices from 1 to 1.33441. (b) The lasing wavelength for even-like and odd-like modes as function of environmental refractive index. The measured R_n of the even-like and odd-like modes are 110 and 99 nm/*RIU* respectively.

Lasing spectra of even-like and odd-like modes when n = 1 are shown in Fig 4-10(a). When the environmental refractive index is varied from 1 to 1.33441, significant linear red-shift in lasing wavelength of even-like and odd-like modes are observed, as shown in Fig. 4-10(a). In Fig. 4-10(b), the measured R_n for the even-like and odd-like modes are 110 and 99 nm/*RIU* respectively. Considering the measured spectral linewidth for these two modes are 0.17 and 0.18 nm respectively, whose corresponds to the Δn_{det} is of 1.5×10^{-3} and 1.8×10^{-3}. Moreover, the simulated R_n of even-like and odd-like modes are 116 and 104 nm/*RIU*, which shows good matches with the measurement results. We also investigate the influence of beam gap on R_n, as shown in Fig. 4-11(a). When the beam gap decreases, R_n of the even-like mode can be improved due to the further enhancement of electric field in the beam gap region. However, R_n of odd-like mode slightly decreases because the electric field distribution in beam gap is slightly suppressed, as illustrated in Figs. 4-5(b) and 4-6(b). It can also be illustrated by introducing the confinement factor γ_{air} to evaluate the field distribution extended to the environmental medium (air). The definition of γ_{air} is shown in the following:

$$\gamma_{air} = \frac{\int_{air} |E|^2 \, dV}{\int_{-\infty}^{\infty} |E|^2 \, dV} \qquad (4\text{-}3)$$

Larger γ_{air} represents more field distribution extending into the air region. Comparing Fig. 4-11(a) with Fig. 4-11 (b), we found that R_n shows strong dependence with γ_{air} and higher γ_{air} would lead higher R_n. It is the field distribution extending into the air region that determines the sensing ability of optical sensor. The sensing ability of single NB is also investigated and noted as the dotted lines in Figs. 4-11(a) and (b). The simulated R_n is always higher in the even mode of coupled-NB than in the 0th-mode of single-NB. Therefore, the *1D PhC* coupled-NB nanocavity would be a better choice for optical sensing rather than *1D PhC NB* nanocavity. In addition, we also compare R_n of the symmetric and asymmetric *1D PhC* coupled-NB nanocavities with $g = 50$ nm. The simulated result show no difference in R_n because their electric field distributions are very similar, as shown in Figs. 4-3(a), (b) and 4-6(a), (b). It means the asymmetric structure caused by the fabrication imperfection will not affect the ability of air-centered *1D PhC* coupled-NB nanocavities in optical sensing.
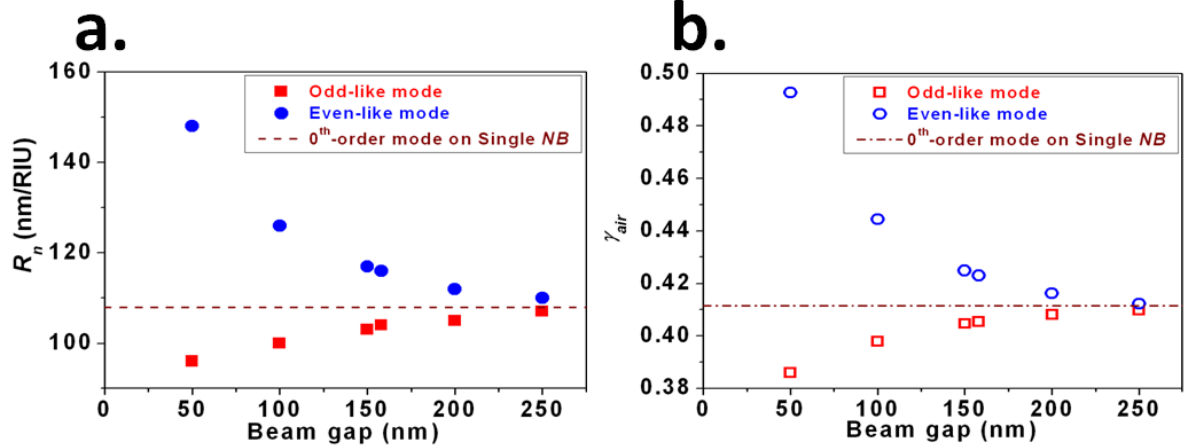
Fig. 4-11: The simulated (a) R_n and (b) γ_{air} as the function of the beam gap.

4.4 Summary

In this chapter, we have investigated the coupled 0th-modes in air-centered *1D PhC* asymmetric coupled-*NB* nanocavities, including even-like and odd-like modes. The asymmetric mode distribution resulted from the asymmetric coupled-*NB* are proved via different spatial non-uniform pump in experiments. For serving as an optical sensor, we have demonstrated the index sensitivity R_n of 110 and 99 nm/RIU from the even-like and odd-like modes, which show good matches with the simulated results. And the measured Δn_{det} from the even-like and odd-like modes are 1.5×10^{-3} and 1.8×10^{-3} respectively. Moreover, we also discover that sensing performance will not be affected by the asymmetric coupled-*NB*.
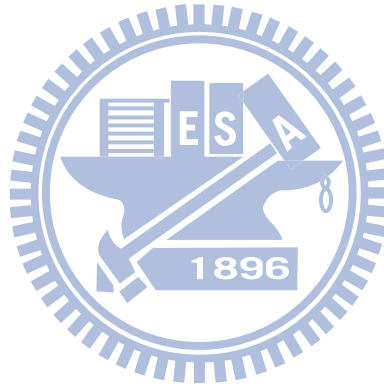
Chapter 5 Conclusion and Future Works

5.1 Conclusion

In this thesis, we have proposed and demonstrated air- and dielectric-centered one-dimensional (*1D*) photonic crystal (*PhC*) nanobeam (*NB*) nanocavity designs. In simulations, the *Q/V* of these two nanocavities are optimized to be 2.9×10^6 $(\lambda/n_{NB})^{-3}$ and 9.9×10^6 $(\lambda/n_{NB})^{-3}$, which will be promising in applications need strong light-matter interactions.

For serving as the efficient nanolaser with ultrasmall device footprint, we applied our nanocavity designs with 8 *GM* periods and the length of total *NB* is only 6 μm. The single mode lasing actions in air- and dielectric-centered *1D PhC NB* nanocavities are both demonstrated. Ultralow lasing threshold of 292 μW is observed from the 0th –order mode in the air-centered *1D PhC NB* nanocavity. The ultra-compact *NB* laser we proposed not only has ultra-small device footprint and low threshold but also has the capability of high-order mode suppression.

For serving as an optical sensor, the air-centered *1D PhC* coupled-*NB* nanocavity is utilized. Although the device is consisted asymmetric couple-*NB* structure, this will not affect its sensing ability according the simulation results. In experiments, the index sensitivity R_n of the even-like and odd-like modes are 110 and 99 nm/*RIU*, which lead to Δn_{det} of 1.5×10^{-3} and 1.8×10^{-3} respectively.

5.2 Future Works

In this thesis, although we have initially demonstrated the nanolaser and optical index sensor, there are several issues worthy to further investigate.

In chapter 3.3.2, the nanolaser is still under pulsed operation. To achieve continuous-wave operation, an underlied low-index substrate will be a good way to reach our goal.

In chapter 4.2, the *1D PhC* coupled-*NB* nanocavity with beam gap < 150 nm has not been achieved, which has strong electric field enhancement and is important for optical sensing. To achieve this, the fabrication processes, including electron beam lithography and dry etching should be carefully optimized. In addition, the utilized mode should also be carefully chosen.

References

[1] E. Yablonovitch, "Inhibited spontaneous emission in solid-state physics and electronics," *Phys. Rev. Lett,* **58**, pp. 2059-2062 (1987).

[2] S. John, "Strong localization of photons in certain disordered dielectric superlattices," *Phys. Rev. Lett.* **58**, pp. 2486-2489 (1987).

[3] S. Y. Lin, J. G. Fleming, D. L. Hetherington, B. K. Smith, R. Biswas, K. M. Ho, M. M. Sigalas, W. Zubrzycki, S. R. Kurtz and Jim Bur, "A three-dimensional photonic crystal operating at infrared wavelengths," *Nature* **394**, pp. 251-253 (1998).

[4] M. Notomi and H. Taniyama, "On-demand ultrahigh-*Q* cavity formation and photon pinning via dynamic waveguide tuning," *Opt. Express* **16**, pp. 18657- 18666 (2008).

[5] Y. Takahashi, H. Hagino, Y. Tanaka1, B. S. Song, Takashi Asano1 and S. Noda, "High-Q nanocavity with a 2-ns photon lifetime," *Opt. Express* **15**, pp. 17206- 17213 (2007).

[6] H. S. Ee, K. Y. Jeong, M. K. Seo, Y. H. Lee, and H. G. Park, "Ultrasmall square-lattice zero-cell photonic crystal laser," *Appl. Phys. Lett.* **93**, pp. 011104 (2008).

[7] H. J. Kimble "Strong interactions of single atoms and photons in cavity QED," *Physica Scripta* **T76**, pp. 127- 137 (1998).

[8] Z. L. Yuan, E. Kardynal, R. Stevenson, J. Shields, J. Lobo, K. Cooper, S. Beattie, A. Ritchie, and M. Pepper, "Electrically driven single-photon source," *Science* **295**, pp. 102-105 (2002).

[9] H. G. Park, S. H. Kim, S. H. Kwon, Y. G. Ju, J. K. Yang, J. H. Baek, S. B. Kim and Y. H. Lee, "Electrically Driven Single-Cell Photonic Crystal Laser," *Science* **305**, pp. 1444-1447 (2004).

[10] K. Nozaki, S. Kita and T. Baba, "Room temperature continuous wave operation and controlled spontaneous emission in ultrasmall photonic crystal nanolaser," *Opt. Express* **15**, pp. 7506- 7514 (2007).

[11] A. D. Falco, L. O'Faolain and T. F. Krauss, "Chemical sensing in slotted photonic crystal heterostructure cavities," *Appl. Phys. Lett.* **94**, pp. 063503 (2009).

[12] S. Kita, K. Nozaki and T. Baba, "Refractive index sensing utilizing a cw photonic crystal nanolaser and its array configuration," *Opt. Express* **16**, pp. 8174- 8180 (2008).

[13] T. Tanabe, K. Nishiguchi, A. Shinya, E. Kuramochi, H. Inokawa and M. Notomi, "Fast all-optical switching using ion-implanted silicon photonic crystal nanocavities," *Appl. Phys. Lett.* **90**, pp. 031115 (2007).

[14] D. O'Brien, M. D. Settle, T. Karle, A. Michaeli, M. Salib and T. F. Krauss, "Coupled photonic crystal heterostructure nanocavities," *Opt. Express* **15**, pp. 1228- 1233 (2007).

[15] B. K. Min, J. E. Kim and H. Y. Park, "High-efficiency surface-emitting channel drop filters in two-dimensional photonic crystal slabs," *Appl. Phys. Lett.* **86**, pp. 011106 (2005).

[16] H. Takano, B. S. Song, T. Asano and S. Noda, "Highly efficient multi-channel drop filter in a two-dimensional hetero photonic crystal," *Opt. Express* **14**, pp. 3491- 3496 (2006).

[17] C. Sauvan, G. Lecamp, P. Lalanne and J. P. Hugonin, "Modal-reflectivity enhancement by geometry tuning in Photonic Crystal microcavities," *Opt. Express* **13**, pp. 245- 255 (2005).

[18] Y. Akahane, T. Asano, B. S. Song, and S. Noda, "High-Q photonic nanocavity in a two-dimensional photonic crystal," *Nature* **425**, pp. 944-947 (2003).

[19] B. S. Song, S. Noda, T. Asano and Y. Akahane, "Ultra-high-Q photonic double-heterostructure nanocavity," *Nat. Mater.* **4**, pp. 207-210 (2005).

[20] P. T. Lee, T. W. Lu, C. M. Yu and C. C. Tseng, "Photonic crystal circular-shaped microcavity and its uniform cavity-waveguide coupling property due to presence of whispering gallery mode," *Opt. Express* **15**, pp. 9450- 9457 (2007).

[21] M. Fujita and T. Baba, "Microgear laser," *Appl. Phys. Lett.* **80**, pp. 2051-2053 (2002).

[22] E. Kuramochi, H. Taniyama, T. Tanabe, A. Shinya and M. Notomi, "Ultrahigh-*Q* two-dimensional photonic crystal slab nanocavities," *Appl. Phys. Lett.* **93**, pp. 111112 (2008).

[23] J. S. Foresi, P. R. Villeneuve, J. Ferrera, E. R. Thoen, G. Steinmeyer, S. Fan, J. D. Joannopoulos, L. C. Kimerling, Henry I. Smith and E. P. Ippen, "Photonic-bandgap microcavities in opticalwaveguides ," *Nature* **390**, pp. 143-145 (1997).

[24] M. Notomi, E. Kuramochi and H. Taniyama, "Ultrahigh-*Q* Nanocavity with 1D Photonic Gap," *Opt. Express* **16**, pp. 11095-11102 (2008).

[25] B. H. Ahn, J. H. Kang, M. K. Kim, J. H. Song, B. Min, K. S. Kim and Y. H. Lee, "One-dimensional parabolic-beam photonic crystal laser," *Opt. Express* **18**, pp. 5654-5660 (2010).

[26] Y. Gong, B. Ellis, G. Shambat, T. Sarmiento, J. S. Harris and J. Vuckovic "Nanobeam photonic crystal cavity quantum dot laser," *Opt. Express* **18**, pp. 8781- 8789 (2010).

[27] Y. Zhang, M. Khan, Y. Huang, J. Ryou, P. Deotare, R. Dupuis and M. Lončar, "Photonic crystal nanobeam lasers," *Appl. Phys. Lett.* **97**, pp. 051104 (2010).

[28] Y. Halioua, A. Bazin, P. Monnier, T. J. Karle, I. Sagnes, G. Roelkens, D. V. Thourhout, F. Raineri and R. Raj, "III-V photonic crystal wire cavity laser on silicon wafer," *J. Opt. Soc. Am.* B **27**, pp. 2146-2150 (2010).

[29] Y. Halioua, A. Bazin, P. Monnier, T. J. Karle, G. Roelkens, I. Sagnes, R. Raj and F. Raineri, "Hybrid III-V semiconductor/silicon nanolaser," *Opt. Express* **19**, pp. 9221-9231 (2011).

[30] R. Perahia, J. D. Cohen, S. Meenehan, T. P. Mayer Alegre and O. Painter, "Electrostatically tunable optomechanical "zipper" cavity laser," *Appl. Phys. Lett.* **97**, pp. 191112 (2010).

[31] Q. Quan, P. B. Deotare and M. Loncar, "Photonic crystal nanobeam cavity strongly coupled to the feeding waveguide," *Appl. Phys. Lett.* **96**, pp. 203102 (2010).

[32] I. W. Frank, P. B. Deotare, M. W. McCutcheon and M. Loncar, "Programmable photonic crystal nanobeam cavities," *Opt. Express* **18**, pp. 8705- 8712 (2010).

[33] X. Chew, G. Zhou, F. S. Chau, J. Deng, X. Tang and Y. C. Loke, "Dynamic tuning of an optical resonator through MEMS-driven coupled photonic crystal nanocavities," *Opt. Lett.* **35**, 2517-2519 (2010).

[34] B. Wang, M. A. Dündar, R. Nötzel, F. Karouta, S. He and Rob W. van der Heijden, "Photonic crystal slot nanobeam slow light waveguides for refractive index sensing," *Appl. Phys. Lett.* **97**, pp. 151105 (2010).

[35] K. Yee, "Numerical solution of initial boundary value problems involving Maxwell's equations in isotropic media," *IEEE Trans. Antennas and Propagation* **14**, pp. 302-307 (1966)

[36] J. Jin, "The Finite Element Method in Electromagnetics," *2nd edition, Wiley, New York,* (2002)

[37] A. R. Clawson, "Guide to references on III±V semiconductor chemical etching," *Materials Science and Engineering* **31**, pp. 1-438 (2001)

[38] G. Johnson, S. Fan, A. Mekis, and J. D. Joannopoulos, "Multipole-cancellation mechanism for high-Q cavities in the absence of a complete photonic band gap," *Appl. Phys. Lett.* **78**, pp. 3388-3390 (2001)

[39] C. Ciminelli, C. M. Campanella, ,and M. N. Armenise, "Simulation and Fabrication of a New Photonic Biosensor," *International Conference on Transparent Optical Networks* , **Tu.P.16** (2010)

Vita

Li-Hsun Chiu was born on 29, January, 1988 in I-lan, Taiwan. He received the B. S. degree from the Department of Biomedical Engineering and Environmental Sciences, National Tsing Hua University (NTHU), Hsinchu, Taiwan, in 2009 and the M. S. degree from the Display Institute, National Chiao Tung University (NCTU), Hsinchu, Taiwan, in 2010. His research was focused on photonic crystal nanocavity.

Publications:

[1] Tsan-Wen Lu, Shao-Pin Lu, **Li-Hsun Chiu**, and Po-Tsung Lee, "Square lattice photonic crystal surface mode lasers," *Opt. Express,* 18, pp. 26461-26468 (2010).

[2] **Li-Hsun Chiu**, Tsan-Wen Lu, Shao-Ping Lu, and Po-Tsung Lee, "Ultra-compact one-dimensional photonic crystal nanobeam laser," OPT1-O-02, *OPT'10*, Tainan, Taiwan (2010). (Best Student Oral Paper Award)

[3] **Li-Hsun Chiu**, Tsan-Wen Lu, Shao-Ping Lu, and Po-Tsung Lee, "Emitting from Wire: One-Dimensional photonic crystal nanobeam Lasers," SC-11, *SNDT'11*, Hsinchu, Taiwan (2011).

[4] Tsan-Wen Lu, **Li-Hsun Chiu**, Pin-Tso Lin, and Po-Tsung Lee, "One-dimensional photonic crystal nanobeam lasers on a flexible substrate," *Appl. Phys. Lett.*, 99, pp. 071101 (2011).